Received: 26 March 2017 | Revised: 25 October 2017 | Accepted: 25 October 2017
DOI: 10.1002/eqe.3004

RESEARCH ARTICLE

WILEY

Experimental study of deformable connection consisting of friction device and rubber bearings to connect floor system to lateral force resisting system

Georgios Tsampras[1] | Richard Sause[2] | Robert B. Fleischman[3] | José I. Restrepo[4]

[1] Simpson Gumpertz & Heger Inc, Waltham, MA, USA
[2] ATLSS Engineering Research Center, Department of Civil and Environmental Engineering, Lehigh University, Bethlehem, PA, USA
[3] Department of Civil Engineering and Engineering Mechanics, University of Arizona, Tucson, AZ, USA
[4] Department of Structural Engineering, University of California, San Diego, CA, USA

Correspondence
Georgios Tsampras, Staff II—Engineering Mechanics and Infrastructure, Simpson Gumpertz & Heger Inc, Waltham, MA, USA.
Email: tsampras.g@gmail.com

Funding information
National Science Foundation, Grant/Award Numbers: CMMI-0402490 and CMMI-1135033

Summary

This paper presents experimental and numerical studies of a full-scale deformable connection used to connect the floor system of the flexible gravity load resisting system to the stiff lateral force resisting system (LFRS) of an earthquake-resistant building. The purpose of the deformable connection is to limit the earthquake-induced horizontal inertia force transferred from the floor system to the LFRS and thereby to reduce the horizontal floor accelerations and the forces in the LFRS. The deformable connection that was studied consists of a friction device (FD) and carbon fiber-reinforced laminated low-damping rubber bearings (RB), denoted as the FD + RB connection.

The test results show that the force-deformation responses of the FD + RB connection are stable under quasi-static sinusoidal and earthquake loading histories and dynamic sinusoidal loading histories. The FD + RB connection force-deformation response is approximated with a bilinear elastic-plastic force-deformation response with kinematic hardening. The FD is axially stiff, compact, easy-to-assemble, and able to accommodate the FD + RB connection kinematic requirements. The FD elastic stiffness controls the FD + RB connection elastic stiffness. The FD friction force controls the force when the FD + RB connection force-deformation response transitions from elastic to post elastic. The RB provide predictable and reliable post-elastic stiffness to the FD + RB connection. The machining tolerances for the FD components, the "break-in" effect, the sliding history, and the dwell time affect the FD friction force. Numerical simulation results for a 12-story reinforced concrete wall building with FD + RB connections under seismic loading show that a reduction of the FD friction force increases the FD + RB connection deformation demand.

KEYWORDS
carbon fiber-reinforced laminated low-damping rubber bearings, deformable connection, floor accelerations, friction device, full-scale dynamic experimental validation

1 | INTRODUCTION

The development of a deformable connection between the floor system of a flexible gravity load resisting system (GLRS) and the stiff lateral force resisting system (LFRS) of an earthquake-resistant building was presented in Tsampras et al.[1] The deformable connection described in Tsampras et al[1] consists of a limited-strength hysteretic component and low-damping laminated rubber bearings. The limited-strength hysteretic component transfers lateral force from the floor system to the LFRS and maintains the stability of the GLRS. The rubber bearings maintain the out-of-plane stability of the LFRS and provide additional post-elastic stiffness to the deformable connection. The use of a deformable connection instead of an essentially rigid-elastic connection at each floor of an example 12-story reinforced concrete shear-wall earthquake-resistant building was shown to limit the earthquake-induced horizontal inertia forces transferred from the floor system to the LFRS and to reduce the floor accelerations.[1] The use of deformable connections also significantly reduces the dispersion (due to the variability of the characteristics of the ground motions) in the peak forces transferred from the floor systems to the LFRS, in the peak floor accelerations, and in the peak LFRS story shears.[1] Results from numerical earthquake simulations of the 12-story reinforced concrete shear-wall earthquake-resistant building presented in Tsampras et al[1] provide the following 4 approximate target properties for a full-scale deformable connection: (a) strength (ie, limiting force) in the range of 800 kN to 1600 kN, (b) elastic stiffness in the range of 200 kN/mm to 2000 kN/mm, (c) post-elastic stiffness of approximately 8 kN/mm, and (d) an approximate upper limit of connection deformation demand of 100 mm.

The deformable connection that is studied in this paper consists of a friction device (FD) and carbon fiber-reinforced laminated low-damping rubber bearings (RB), denoted as the FD + RB connection. Figure 1 shows a schematic example of a reinforced concrete shear-wall earthquake-resistant building with FD + RB connections. The paper presents details of an FD + RB connection test specimen. Detailed test results for the FD + RB connection are presented. The experimental response of the FD, which dominates the FD + RB connection force-deformation response, is discussed extensively, and the paper presents results from preliminary experimental studies of FD force variation, which compare low levels of FD force versus high levels of FD force, and machined steel FD components with tight tolerances versus steel FD components with mill-quality surfaces and looser tolerances. The paper also presents more detailed information about FD force variation observed in quasi-static and dynamic tests and the relationship of the FD force variation to the FD interface sliding history. Finally, a validated, reasonably accurate model for the FD + RB connection force-deformation response is presented. Results from limited numerical simulations using this model are presented to assess the effects of potential FD force variations on the seismic response of a 12-story reinforced concrete shear-wall building model.

2 | EXPERIMENTAL SETUP

Figure 2 shows the experimental setup used to test the FD + RB connection. A simulated floor system and a reinforced concrete shear wall (ie, the LFRS) were built in the laboratory. The south end of the FD was attached to the wall. The

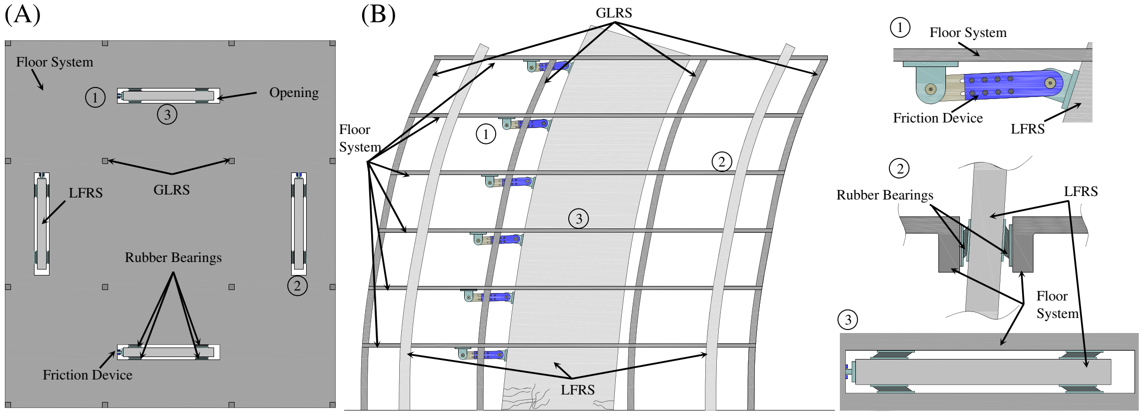

FIGURE 1 Friction device (FD) + rubber bearings (RB) deformable connection within reinforced concrete shear-wall building: A, plan view; B, elevation and close-up of (1) relative vertical motion between lateral force resisting system (LFRS) (ie, shear wall) and floor, (2) relative rotation between LFRS and floor, and (3) relative horizontal motion between LFRS and floor [Colour figure can be viewed at wileyonlinelibrary.com]

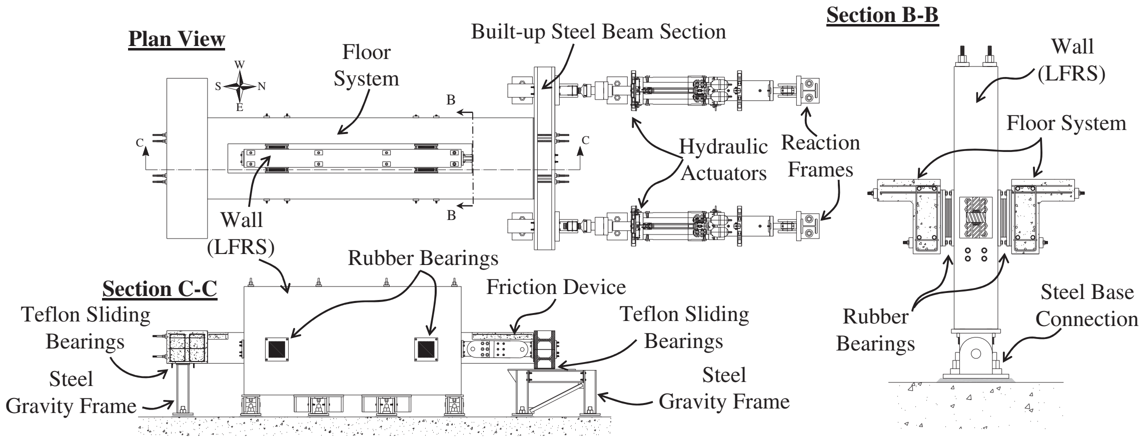

FIGURE 2 Full-scale friction device (FD) + rubber bearings (RB) test setup

north end of the FD was attached to a built-up steel beam, which was part of the simulated floor system. Clevis connections with spherical bearings in each end of the FD were used to attach the FD to the wall and the floor system. The FD + RB connection was deformed by subjecting the floor system to predefined displacement (relative to the wall) histories in the north-south direction, using hydraulic actuators that were supported by a steel reaction frame at the north end and the built-up steel beam at the south end. The built-up steel beam was post-tensioned to the floor system. The weight of the floor system was supported on Teflon slide bearings. The wall base was attached to the laboratory strong floor through a steel connection. The RB are shown in section B-B. One side of each one of the RB is attached to the floor system, and the other side of the RB is attached to the wall by using threaded rods. The motion of the floor system in the north-south direction deformed the FD axially and deformed the RB in shear. The FD was in tension when the actuators were retracted toward the north and in compression when the actuators were extended toward the south. A description of the test setup details is presented in Tsampras and Sause.[2] Shake table tests[3,4] show that the FD + RB connection meets all kinematic requirements shown in Figure 1.

3 | LAMINATED LOW-DAMPING RUBBER BEARINGS

The purpose of the RB is to provide post-elastic stiffness to the FD + RB deformable connection and to maintain the out-of-plane stability of the LFRS. Laminated low-damping RB were selected for this purpose because they have nearly linear elastic response under large shear deformations,[5-8] and they have significant compressive stiffness, which is needed to maintain the out-of-plane stability of the LFRS. The mechanical properties of the RB are not expected to be shear deformation rate dependent.[6] Because the RB are located inside the building, low-temperature effects on the shear force-deformation response[5] are neglected. More specifically, carbon fiber-reinforced laminated low-damping RB were selected for the rubber bearing components in the FD + RB. This section presents the design, installation, instrumentation, and experimental response of the RB.

3.1 | Design, installation, and instrumentation

Each one of the RB consists of carbon fiber-reinforced rubber layers attached to 2 steel end-plates. The rubber is 50 ± 5 Duro Gr 3 with shear modulus $G = 0.9$ MPa, based on the upper bound of G provided by AASHTO.[9] The critical design parameter for the RB was a target post-elastic stiffness for the FD + RB connection. As mentioned earlier, based on Tsampras et al,[1] the target FD + RB connection post-elastic stiffness is approximately 8 kN/mm, and the FD + RB connection design deformation, which equals the RB design shear deformation, is $D_{\mathrm{RB},d} = 100$ mm. The shear strain γ limit for elastic response of laminated low-damping RB is between 100% and 200%.[5-7] Assuming the shear strain design limit is $\gamma_d = 200\%$, the required total thickness of the rubber layers in the RB is $h_{rt} = D_{RB,d}/\gamma_d = 50$ mm. Table 1 lists the dimensions and the expected properties of 1 of the RB. W and L are the plan dimensions of the rubber bonded to the steel end-plates, h_{rt} is the total thickness of the rubber layers, n_L is the number of rubber layers, S is the shape factor of the rubber layers, K_{RB} is the shear stiffness of 1 of the RB. E_c is the compressive modulus of the RB, and K_c is the compressive stiffness of 1 of the RB.

TABLE 1 Dimensions and nominal properties of 1 rubber bearing

W	L	h_{rt}	n_L	$h_{\mathrm{ri}} = h_{\mathrm{ri}}/n_L$	$S = A/[2h_{\mathrm{ri}}(W + L)]$	G	$K_{\mathrm{RB}} = \mathrm{GA}/h_{rt}$	$E_c = 6\mathrm{GS}^2$	$K_c = E_cA/h_{rt}$
[mm]	[mm]	[mm]	[–]	[mm]	[–]	[MPa]	[kN/mm]	[MPa]	[kN/mm]
356	356	50	4	12.5	7	0.9	2.2	264	656

Note: Area of the rubber $A = WL$

The 4 RB in the FD + RB connection have a total expected shear stiffness of $4K_{\mathrm{RB}} = 8.8$ kN/mm. Shear and compressive strain checks related to combined compression, rotation, and shear due to the kinematic requirements shown in Figure 1 were performed considering the AASHTO specifications[9,10] and references.[11,12]

Figure 3A shows an overview of 2 RB on the west side of the wall and the linear variable differential transformers (LVDTs) used to measure the shear deformation of the RB. The average measurement from 4 LVDTs positioned (1 each) at the 4 RB is taken as the RB shear deformation. The RB shear strain is calculated by dividing the RB shear deformation by h_{rt}. The total RB force (total shear force of the 4 RB) was measured indirectly by subtracting the measured force in the FD from the sum of the forces in the 2 actuators. As a result, the total RB force includes a small friction force, approximately 30 kN, developed between the Teflon slide bearings and the steel gravity frames shown in Figure 2A. Figure 3B shows a close-up view of 1 of the RB and a typical linear potentiometer installed between the rubber bearing steel end-plate and the wall to measure the potential slip of the end-plate relative to the wall. Similar linear potentiometers were used to measure the potential slip of each rubber bearing steel end-plate relative to the floor system.

Figure 3C to F shows the installation steps followed for each rubber bearing. The first step was to bolt an rubber bearing steel end-plate to the face of the wall. The smooth wall concrete surface ensured good contact between this steel end-plate and the wall. Wooden edges were driven into the space between the other rubber bearing steel end-plate and the floor system to precompress the rubber bearing against the wall. An approximate average compressive strain equal to 0.3% (or approximately 0.6 MPa calculated compressive stress) developed in the rubber bearing from driving the wedges. Grout was used between the rubber bearing steel end-plate and the floor system to ensure good contact and maintain the precompression. Finally, the rubber bearing steel end-plate was bolted on the floor system. Figure 3G shows an installed rubber bearing.

3.2 | Experimental observations

One set of RB was used throughout the experiments, and the RB were new at the beginning of test 1. Figure 4A shows the total RB force-shear strain response observed in test 1 and the RB deformation time history. The effective stiffness and the effective viscous damping ratio ξ, as defined in Constantinou et al and AASHTO,[5,10] are typically used to characterize the response of RB. In Figure 4A, the effective stiffness for the set of 4 RB, K_{eff}, calculated from the data for the 3 constant

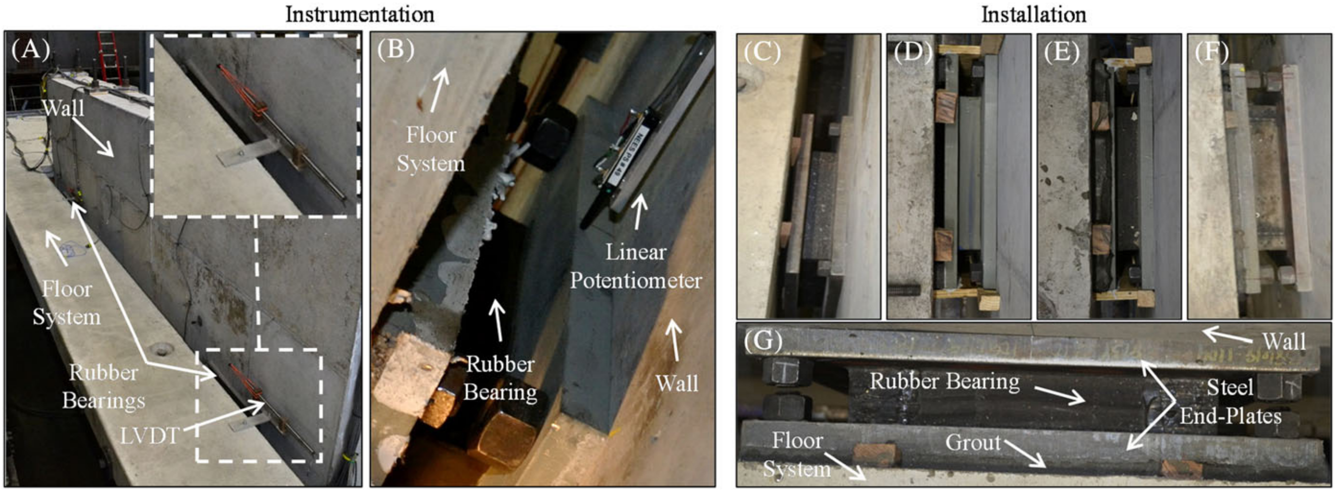

FIGURE 3 A, Overview of 2 rubber bearings (RB) with linear variable differential transformers (LVDTs) to measure shear deformation; B, typical linear potentiometer used to measured potential slip of the steel end-plate relative to wall; C to F, installation steps for 1 rubber bearing; G, close-up view of installed rubber bearing [Colour figure can be viewed at wileyonlinelibrary.com]

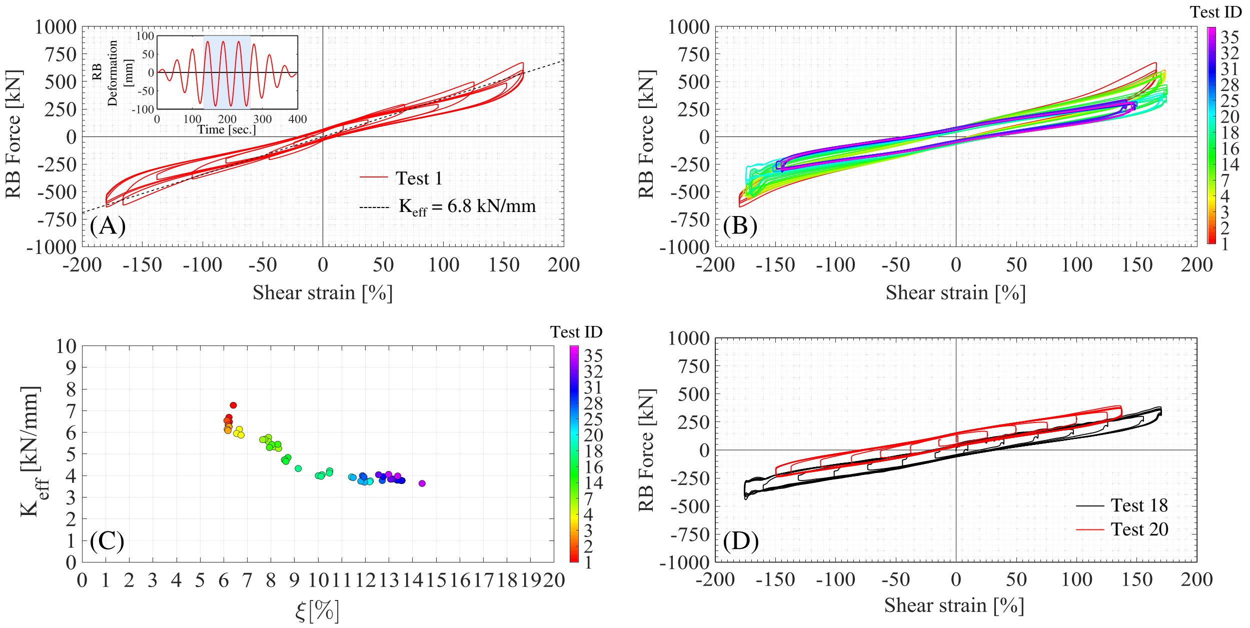

FIGURE 4 A, Test 1 total rubber bearings (RB) force-shear strain, K_{eff}, and RB deformation time history; B, total RB force-shear strain; C, K_{eff} versus ξ; D, total RB force-shear strain in tests 18 and 20 to demonstrate the residual total RB force due to severe damage in test 20 [Colour figure can be viewed at wileyonlinelibrary.com]

amplitude cycles at ±89 mm RB shear deformation (ie, ±175% shear strain) is shown to be 6.8 kN/mm. This observed K_{eff} is close to $4K_{\text{RB,lower bound}} = 6.5$ kN/mm, calculated by using a lower value of $G = 0.66$ MPa provided in AASHTO.[9] The reduction in the peak total RB force from the fourth to the fifth cycle was 10%, and the reduction in the peak total RB force from the fifth to the sixth cycle was 3%. Figure 4B shows the total RB force-shear strain observed in the constant amplitude cycles of selected quasi-static sinusoidal tests, with 3 or 6 peak amplitude cycles that lead to peak shear strains from 150% to 175%. After a large number of cycles (ie, significantly larger than the number of cycles expected in a design basis earthquake, DBE) at large shear strains, the total reduction of K_{eff} was approximately 40%, which is associated with tearing and debonding of the rubber from the steel-end plates. Figure 4C shows K_{eff} versus ξ. The observed increase in ξ is attributed to friction that develops due to the tearing and debonding of the RB. Slippage of 1 of the 4 bearings relative to the wall occurred in test 20, which resulted in residual total RB force at 0 shear strain of approximately 80 kN. Figure 4D shows the shifted total RB force-shear strain response in test 20 compared with test 18. The residual total RB force has been subtracted in all other plots to allow a comparison of the results. Figure 5A to D compares the total RB force-shear strain response under quasi-static and dynamic loading histories. These figures show that the total RB force-shear strain response is essentially unaffected by the loading frequency of the displacement histories applied in the testing program.

4 | FRICTION DEVICE

Friction devices for structural engineering applications have been tested in the past. Clark et al (1973) presented test results for a static load control FD intended to limit the effect of differential settlement that occurs at foundations.[13] Other researchers used FDs for energy dissipation in various types of earthquake-resistant structures (ie bridge structures,[14] precast concrete structures,[15-19] steel braced frames,[20-30] steel moment resisting frames,[31] self-centering moment resisting frames,[32-37] and rocking timber shear walls[38]). Friction dampers[39-43] and self-centering braces with friction-based energy dissipation[44-47] have been developed and tested.

This section shows the development of an FD that is used as limited-strength hysteretic component in the FD + RB connection. The FD + RB connection requires an axially stiff, compact, and easy-to-assemble FD, which accommodates the kinematic requirements shown in Figure 1. The design and instrumentation of the FD developed for the FD + RB connection are presented. The expected differences between an idealized Coulomb type FD force-deformation response and a realistic FD force-deformation response are discussed by using schematic examples. Experimental results from quasi-static

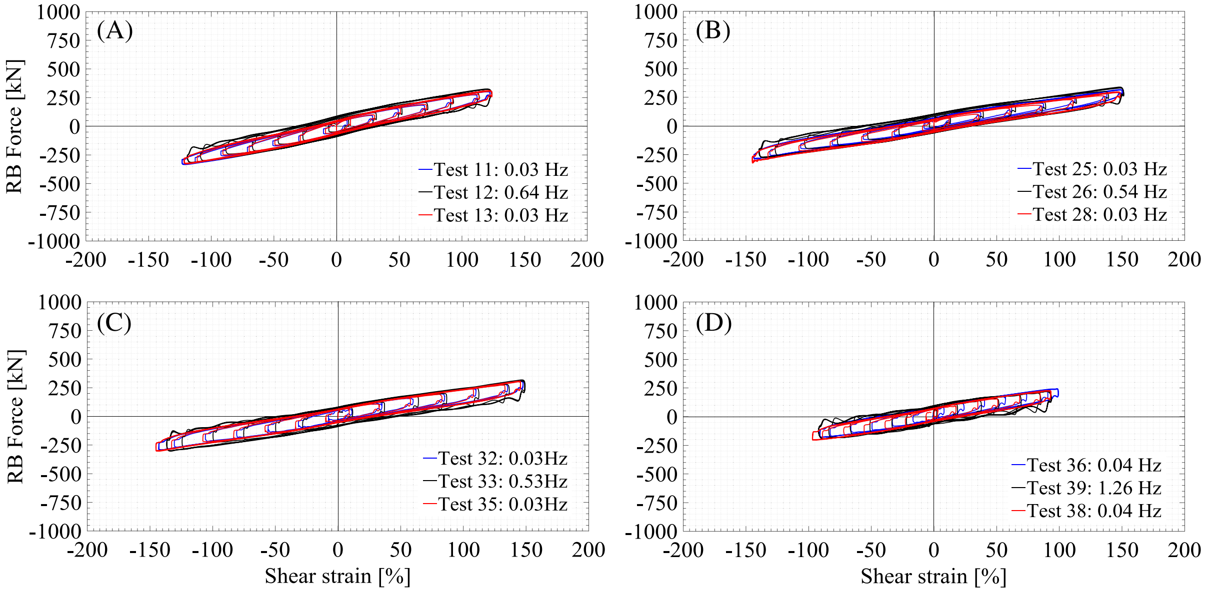

FIGURE 5 Total rubber bearings (RB) shear force-strain response under quasi-static and dynamic loading histories [Colour figure can be viewed at wileyonlinelibrary.com]

sinusoidal and earthquake displacement control tests, dynamic sinusoidal displacement control tests, and shake-table earthquake tests are used to demonstrate the parameters that affect the FD force-deformation response.

4.1 | Friction device design and instrumentation

Figure 6A shows the full-scale FD and its components. Two outer steel plates, 1 middle steel plate, and 2 friction shims are clamped by using ASTM A325 bolts that are denoted as "friction bolts." The FD has 2 friction (sliding) interfaces between the middle steel plate and the 2 friction shims. The friction bolts pass through standard holes[48] in the outer steel plates and the friction shims. These standard holes have 1.6-mm (ie, 1/16 in) larger diameter than the diameter of the friction bolts. Slots in the middle steel plate allow the friction bolts, the outer steel plates, and the friction shims to move relative to the middle steel plate (sliding occurs between the friction shims and the inner steel plate). Clevis plates with spherical bearings were used to accommodate the kinematic requirements shown in Figure 1 and to prevent out-of-plane forces (acting normal to the sliding interfaces) from developing in the FD. The existing test setup required the use of identical clevis connections at each end of the FD. As a result, a fixed bolted connection was required in the FD, as shown in Figure 6A. Section 4.3.3 presents an alternative FD configuration without this fixed bolted connection. The FD is symmetric about the longitudinal axis to prevent out-of-plane forces from developing in the FD.

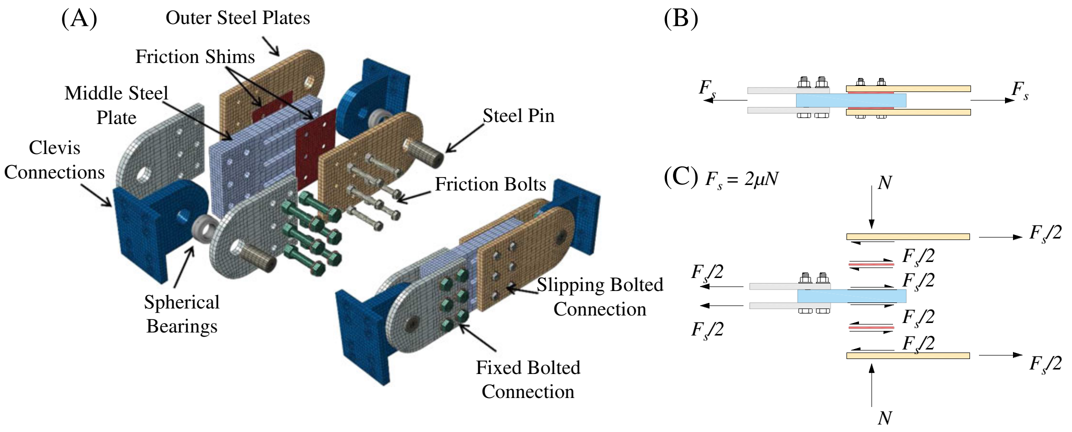

FIGURE 6 A, Full-scale friction device (FD); B and C, idealized free body diagrams [Colour figure can be viewed at wileyonlinelibrary.com]

Figure 6B and C shows idealized free body diagrams of the FD. Assuming that the forces in the RB are small when sliding on the friction interfaces begins, the friction force in the FD controls the force level (ie, strength or limiting force) when the FD + RB connection transitions from elastic to post-elastic force-deformation response. Thus, the target full-scale FD friction force is in the range of 800 kN to 1600 kN. As mentioned earlier, the FD design deformation is close to 100 mm. The friction force can be estimated by using Coulomb theory, $F_s = n_s N \mu_s$, where $n_s = 2$ is the number of friction interfaces, N is the total normal force that the friction bolts apply on the friction interfaces, and μ_s is the friction coefficient. Assuming $\mu_s = 0.3$, $N = 1333$ kN is required to achieve $F_s = 800$ kN. The use of Belleville washers to control the forces applied by the friction bolts was considered; and assuming that 45 kN of force can be developed in each friction bolt by using Belleville washers, a total number of friction bolts $n_b = 30$ is required to achieve $N = 1333$ kN, which is impractical. If standard hardened flat washers are used and friction bolts with diameter $d_b = 25.4$ mm are pretensioned to 227 kN (ie, the minimum pretension load,[48] which is the recommended pretension load when no Belleville washers are used), then $n_b = 6$ is required to achieve $N = 1333$ kN, so $n_b = 6$ is used in the full-scale FD.

Figure 7A shows the FD middle steel plate used in the full-scale tests. The loose mill scale was removed from the FD middle steel plate surfaces. However, to make the FD more economical, the middle steel plate surfaces were not machined, assuming that a stable force-deformation response could be achieved without machined surfaces. Test results shown later in section 4.4 validate this assumption. Figure 7B shows components of the FD. Figure 7C shows the assembled FD, and Figure 7D shows the FD installed in the full-scale test setup. The length of the FD from clevis pin to clevis pin was 1.10 m. The total length from clevis end plate to clevis end plate was 1.6 m. The force in the FD during the experiments, denoted as F_{FD}, was directly measured by using a pin load cell, which was installed at the south clevis of the FD. F_{FD} during sliding on the friction interfaces is denoted as F_{FDs}. Linear variable differential transformers were used to measure the FD deformation, denoted as u_{FD}. u_{FD} during sliding is denoted as u_{FDs}. Figure 7E shows the clevis connection attached to the wall. The use of grout between the clevis connection plate and the wall ensures good contact. Clevises with spherical bearings accommodate the potential for construction imperfections, as well as the kinematic requirements shown in Figure 1. Examples of a clevis accommodating a small misalignment and a large misalignment are shown in Figure 7F and G, respectively.

4.2 | Schematic examples of idealized and realistic friction device force-deformation responses

Figure 8A shows a schematic example u_{FD} time history. Figure 8B shows a schematic example of the idealized F_{FD} response to u_{FD} with a red solid line, and a schematic example of a realistic F_{FD} response to u_{FD} with a green dashed line. Figure 8C shows the schematic F_{FD} versus u_{FD} idealized and realistic responses for a single u_{FD} cycle. The idealized $|F_{\mathrm{FDs}}|$ is assumed to be equal to the friction force from Coulomb theory, ie, $|F_{\mathrm{FDs}}| = F_s = n_s N \mu_s$. The idealized F_{FDs}

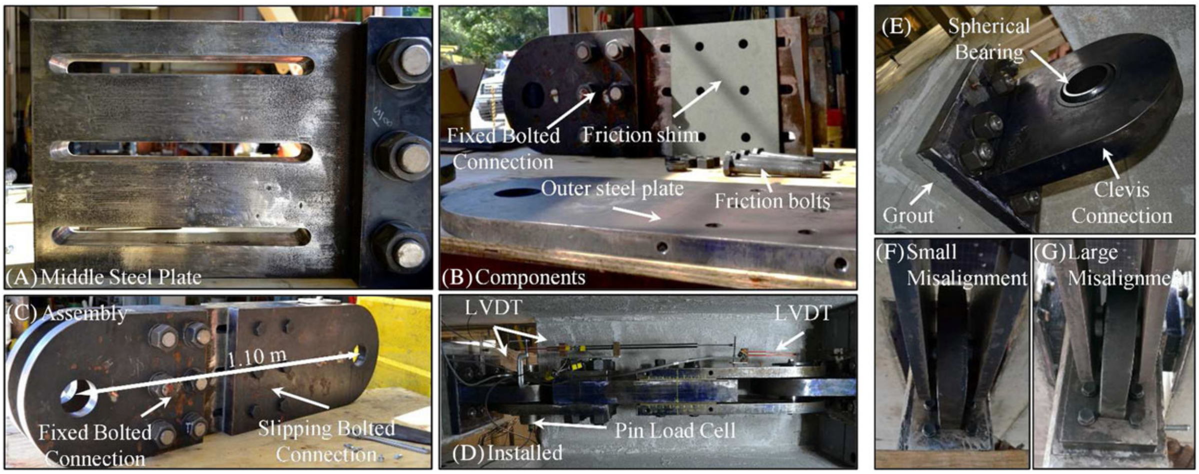

FIGURE 7 A, Surface of middle steel plate; B, friction device (FD) components; C, assembled FD; D, installed FD; E, clevis connection at wall; F, clevis accommodating small misalignment; G, clevis accommodating large misalignment [Colour figure can be viewed at wileyonlinelibrary.com]

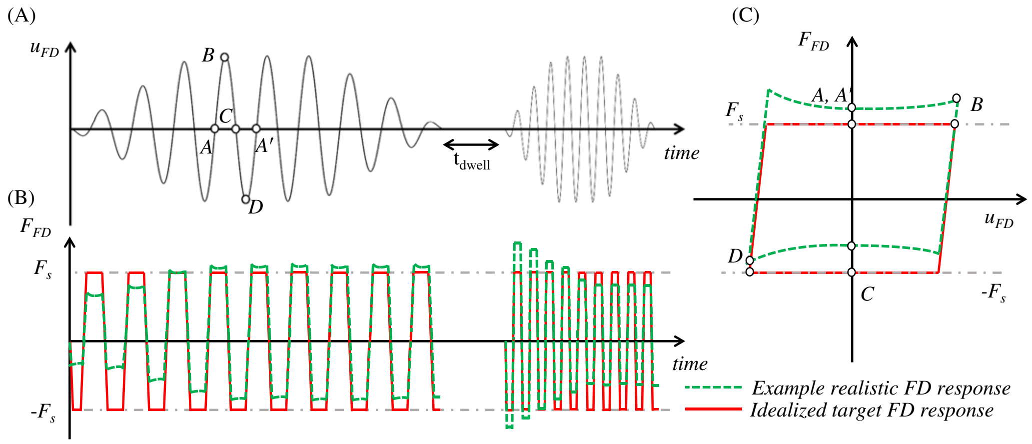

FIGURE 8 Schematic example of idealized and realistic friction device (FD) force versus deformation response [Colour figure can be viewed at wileyonlinelibrary.com]

response is symmetric in tension and in compression and does not vary with u_{FDs}, the rate of u_{FDs}, or the cumulative u_{FDs}. The idealized F_{FDs} is not affected by expected changes in the friction interface initial conditions from wear over time (known as "break-in" effect). The idealized F_{FDs} is not affected by the time over which the 2 interface surfaces are in contact without sliding, noted as "dwell time" denoted as t_{dwell}. Experimental FD force-deformation responses are shown in the following sections in comparison with the idealized F_{FDs}.

4.3 | Preliminary studies

Experimental results from 4 preliminary studies, denoted as PS1, PS2, PS3, and PS4, respectively, are presented in this section. PS1, PS2, and PS3 used the steel components of the FD presented in section 4.1. PS1 compares the FD force-deformation response for 2 different friction shim materials at FD force levels less than that required for the full-scale FD (ie, less than 800 kN). Half-hard brass B36 UNS no. C26000[49] material and AFT200 composite material[50] were used for the friction shims in PS1 because these 2 materials were used in previous FD tests (ie, brass in Grigorian and Popov, Khoo et al, Petty, and Kim and Christopoulos[30-32,35] and AFT200 in Chi and Uang[51]). PS2 and PS3 compare the FD force-deformation response for 2 different FD force levels (by increasing) by using AFT200[50] friction shims. PS4 shows results from shake-table earthquake tests described in Zhang et al and Fleischman et al.[3,4] Table 2 lists information about the 4 preliminary studies.

TABLE 2 Friction device (FD) preliminary study information

Test	[5]N	μ_s	[1]F_s	Belleville Washers	[2]Bronze Friction Bolt Sleeves	Friction Shim Material	Friction Shim Thickness	Type of Test
[–]	[kN]	[–]	[kN]	[–]	[–]	[–]	[mm]	[–]
PS1	134	0.42	113	Yes	Yes	[3]Brass/AFT200	4.8	Quasi-static
PS2	201	0.42	169	Yes	No	[3]AFT200	4.8	Quasi-static
PS3	[4]1040	0.42	874	No	No	[3]AFT200	4.8	Quasi-static
PS4	114	0.42	96	Yes	Yes	AFT200	9.5	Shake-table

[1] $F_s = n_s N \mu_s$, where $n_s = 2$.

[2] Bronze friction bolt sleeves used to avoid direct contact of friction bolts on edges of slots.

[3] PS1, PS2, and PS3 use the same AFT200 friction shim plates. The brass friction shims and the AFT200 friction shims were new at the beginning of PS1.

[4] The use of more friction bolts at higher pretension increased N in PS3 compared with N in PS1 and in PS2.

[5] N was estimated based on the applied torque from the torque-wrench. In PS4, some of the friction bolts were instrumented with strain gages, and for those bolts, the relationship among the axial strain, the axial load, and the torque from the wrench was known.

4.3.1 | Preliminary study PS1

Figure 9A shows the setup used in PS1 and the initial surface conditions of the middle and outer steel plates at the friction interfaces. Figure 9B and C shows the brass friction shim surface condition and AFT200 friction shim surface condition, respectively, before the tests. Figure 9D and E shows the brass friction shim surface condition and AFT200 friction shim surface condition, respectively, after the tests and the middle plate surface condition after the test. Nonuniform wear is observed. On inspection, it was observed that brass particles were adhered to the middle steel plate surface, but AFT200 friction shim particles were not adhered to the middle steel plate surface. Figure 9F shows the FD force-deformation response. The dashed lines represent the friction force from Coulomb theory, $\pm F_s$ (see Table 2). F_{FDs} at u_{FD} of 25 mm is less than F_{FDs} at -75 mm for the brass shims and AFT friction shims. Careful study of the middle steel plate and bronze friction bolt sleeves (see note on Table 2) showed that the friction bolt sleeves were worn by the edges of the slots because the slot edges were not sufficiently straight and parallel. Thus, variation in contact between the bronze friction bolt sleeves and the slot edges, as u_{FD} varied, caused variation in F_{FDs}. Also, a smaller F_{FDs} is observed at u_{FD} of 25 mm for the AFT200 friction shims compared with the brass shims. The "break-in" effect associated with the AFT200 material, which is discussed further in section 4.3.3, explains this difference.

4.3.2 | Preliminary studies PS2 and PS3

Figure 2 shows the test setup used in PS2 and PS3. Figure 10A shows the FD force-deformation response in PS2. F_{FDs} at u_{FD} of 25 mm is approximately 25% less than the F_{FDs} at -75 mm. Thus, the variation of F_{FDs} is smaller in PS2 than the

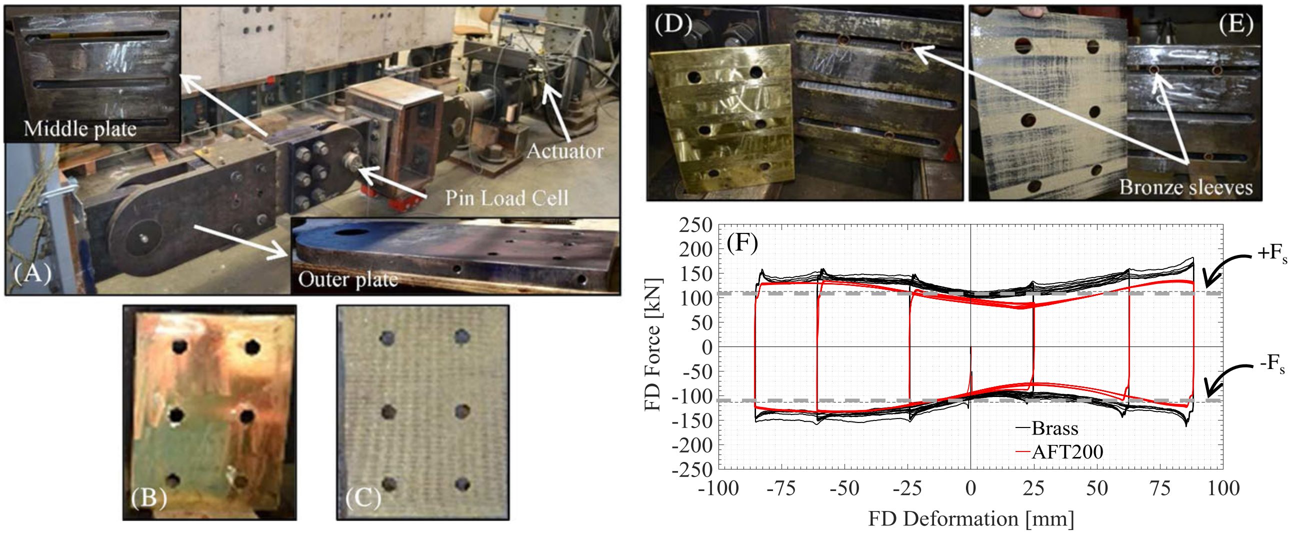

FIGURE 9 Preliminary study PS1: A, test setup; B, brass and C, AFT200 friction shim condition before tests; D, brass and E, AFT200 friction shim condition and middle steel plate surface condition after tests; F, friction device (FD) force-deformation response [Colour figure can be viewed at wileyonlinelibrary.com]

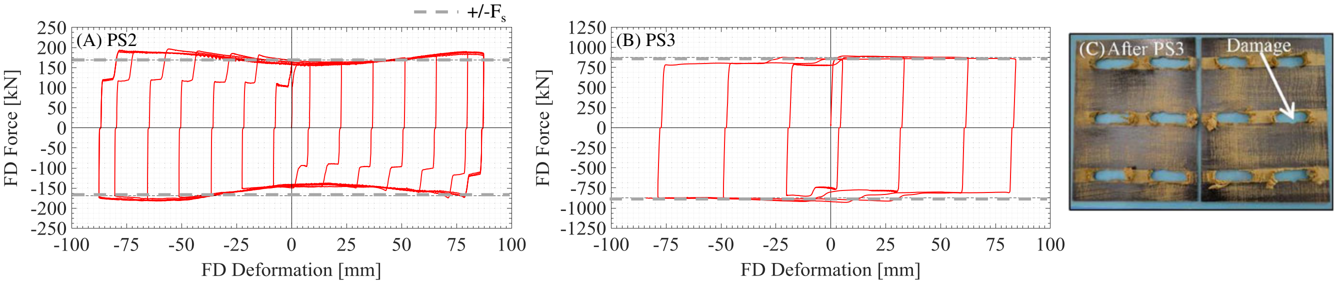

FIGURE 10 Friction device (FD) force-deformation in A, preliminary study PS2 and B, preliminary study PS3; C, condition of friction shims after preliminary study PS3 [Colour figure can be viewed at wileyonlinelibrary.com]

variation of F_{FDs} in PS1. This observation suggests that the variation in F_{FDs} due to the variation in contact between the friction bolts and slot edges, as u_{FD} varies, is less significant relative to the total F_{FDs} when the FD force level increases (see F_s in Table 2). Figure 10B shows the FD force-deformation response in PS3. PS3 used a full-scale FD force level, which is approximately 8 times the FD force level in PS1 (see F_s in Table 2). The variation in F_{FDs} due to the variation in contact between the friction bolts and slot edges was insignificant.

Figure 10C shows the conditions of the AFT200 friction shims after PS3. The damage to the holes of the friction shims is caused by bearing stresses on the edges of the bolt holes under a full-scale FD force level. The idealized free body diagram shown in Figure 6C assumes that $F_s/2$ develops between the middle steel plate and the friction shim and assumes that $F_s/2$ develops between the outer steel plate and the friction shim. This assumption leads to zero net force on the friction shim. However, the friction force at the interface of the friction shim and the middle steel plate differs from the friction force at the interface of the friction shim and the outer steel plate due to different interface conditions (ie, different amount of “break-in” effect). This difference in friction forces between the 2 friction interfaces causes bearing forces and damage of the friction shim bolt holes. The steps in the FD force-deformation responses in Figure 10A and B are related to the friction shim bolt hole damage. Prior to each step, slip occurs at the friction interface with less break-in (ie, between the outer steel plate and the friction shim). The step indicates that the friction bolts begin to bear on the edges of the damaged bolt holes in the friction shim. After bearing of the bolts on the bolt holes, slip occurs at the friction interface with greater break-in (ie, between the middle steel plate and the friction shim). Later (eg, section 4.4), it is shown that the friction shim damage is avoided by increasing the thickness of the friction shims.

4.3.3 | Preliminary study PS4

Four FDs were used in 4 FD + RB connections between the (4) floor systems and the LFRS in the test building used in shake-table tests described in Zhang et al and Fleischman et al.[3,4] As shown in Figure 11, a different clevis connection type was used at each end of the FD, eliminating the fixed bolted connection from the FD shown in Figure 6A. Figure 11A shows the middle steel plate, the outer steel plates, and the AFT200 friction shims of 1 of the FDs. The steel plates were machined with ±0.05 mm (ie, ±0.002 in) tolerance for the surface flatness, −0/+0.13 mm (ie, −0/+0.005 in) tolerance for the diameter of the bolt holes, ±0.08 mm (ie, ±0.003 in) tolerance for the location of the slots, −0/+0.10 mm (ie, −0/+0.004 in) tolerance for the width of the slots, and ±0.10 mm (ie, ±0.004 in) tolerance for the thickness of the plates. Figure 11B shows the 4 assembled FDs with a set of clevis connections. Figure 11C shows part of the test building in which the FDs were installed as part of the FD + RB connections. Figure 11D shows a close-up view of the installed FD.

Figure 12A and C shows the FD force-deformation response of the FD from the fourth and second floors, respectively, during test 14 of the shake-table test program. $\pm F_s$ is shown with dashed lines and is similar to F_s from PS1 (see Table 2). F_{FDs} (ie, shown by the red points in Figure 12A and C) does not vary significantly in PS4 because the machining of the steel plates ensures that the bronze friction bolt sleeves move in the slots without developing significant friction forces. The F_{FDs} in the fourth floor FD is greater than the F_{FDs} in the second floor FD. This difference is attributed to the “break-in” effect. Figure 12B and D shows that the friction coefficient determined from the test data, $\mu_{\mathrm{exp}} = |F_{\mathrm{FDs}}|/2\,N$, increases as the cumulative u_{FDs} increases during the 14 tests. μ_{exp} increases as the cumulative u_{FDs} increases because wear of the surfaces of the friction shims changes the friction interface conditions. Damage to the friction shims was not observed in the FDs used in the shake-table tests.

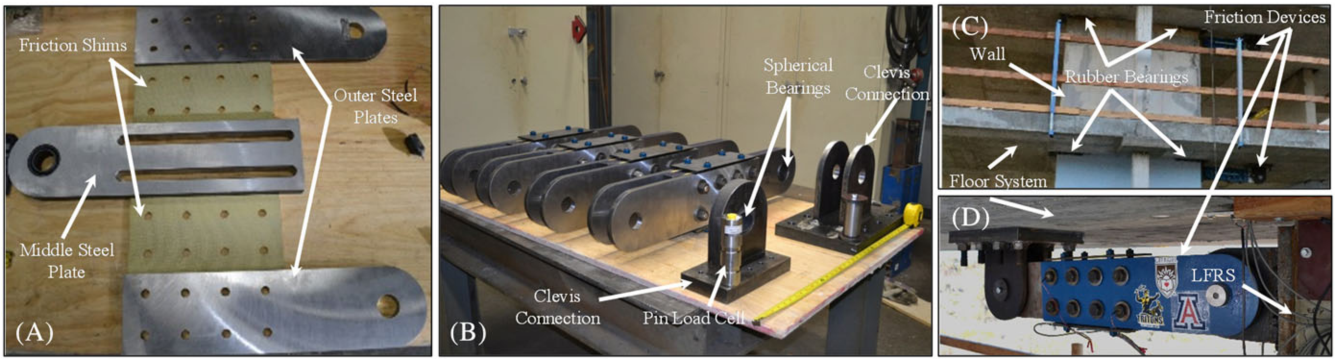

FIGURE 11 Friction device (FD) in shake-table test [Colour figure can be viewed at wileyonlinelibrary.com]

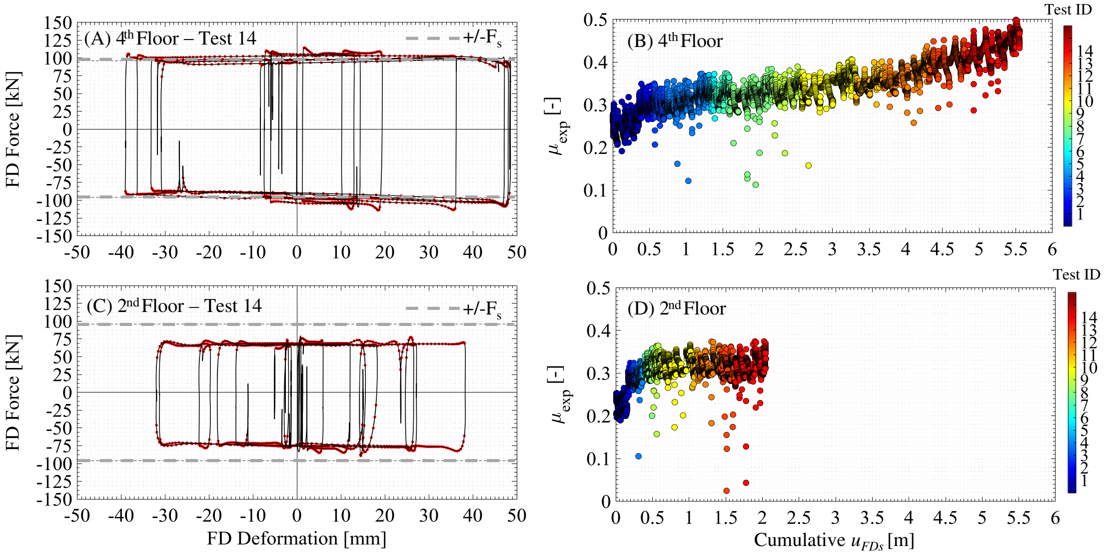

FIGURE 12 Preliminary study PS4: (A and C) friction device (FD) force-deformation response in shake-table test 14; (B and D) μ_{exp} versus cumulative u_{FDs} in shake-table tests 1 through 14 [Colour figure can be viewed at wileyonlinelibrary.com]

4.3.4 | Summary of preliminary studies

PS1 showed that the variation in F_{FDs} due to variation in contact between the bronze friction bolt sleeves and the slot edges is significant in comparison with F_{FDs} when the FD force levels are much less than required for the full-scale FD. PS2 showed that the F_{FDs} variation is less significant relative to the total F_{FDs} when the FD force level is larger. PS3 showed that the F_{FDs} variation is insignificant at full-scale FD force levels. Belleville washers and bronze friction bolt sleeves were not used in PS3. PS3 also showed that the full-scale FD force levels may lead to damage of the friction shims. PS4 showed that, at FD force levels less than the full-scale FD force level, the variation in F_{FDs} is reduced by using tight machining tolerance for the surface flatness, the diameter of the bolt holes, the slot locations, the slot widths, and the thickness of the steel plates. Belleville washers and bronze friction bolt sleeves were used in PS4. A distinct "break-in" effect was observed in PS4.

In summary, the preliminary studies show that (1) an FD with machined steel plates with tight tolerance, with bronze friction bolts sleeves, with Belleville washers, with $|F_{FDs}|$ of approximately 100 kN, and $|u_{FDs}|$ of approximately 50 mm can have stable force-deformation response; (2) an FD with steel plates machined for standard structural applications, without bronze friction bolt sleeves, without Belleville washers, with $|F_{FDs}|$ of approximately 800 kN, and $|u_{FDs}|$ of approximately 80 mm can have stable force-deformation response; (3) the "break-in" effect may lead to significant increase of friction force as the cumulative u_{FDs} increases; and (4) damage of the friction shims can be avoided by increasing their thickness.

4.4 | Full-scale friction device experimental response

This section presents the full-scale tests (Figure 2) that were conducted after completing the preliminary tests. The steel components of the FD presented in section 4.1 were used in the tests discussed in this section. The friction shims were made of the composite material Gatke 398.[52] A nonmetallic material was used for the friction shims to avoid the possibility of galvanic corrosion on the friction interface. Gatke 398 has tensile, compression, and shear strength of 113.8 MPa, 320.6 MPa, and 86.2 MPa, respectively.[52] A friction interface between steel and Gatke 398 is expected to have μ_s in the range of 0.2 to 0.5.[52] The thickness of the friction shims was 9.5 mm. One set of Gatke 398 friction shims was used in tests 30 through 63. Some of the test results are discussed in this section. The friction shims were new at the beginning of test 30. Six ASTM A325 25.4-mm diameter friction bolts were used. Bronze friction bolt sleeves and Belleville washers were not used. The friction bolts were tensioned before test 30 to a total normal force $N = 816$ kN. Assuming $\mu_s = 0.45$, $F_s = 735$ kN. Table 3 lists the loading frequencies for sinusoidal loading histories, t_{dwell}, and the objectives for tests 30 through 45.

TABLE 3 Amplitudes, loading frequencies, test type, t_{dwell}, and objectives for tests 30 through 45

Test	Amplitude	Loading Frequency	Test Type	t_{dwell}	Objective
[−]	[mm]	[Hz]	[−]	[minutes]	[−]
30	70	–	Earthquake	–	Assess force-deformation response under initial conditions for earthquake loading.
31	75	0.03	Sinusoidal	22	Assess force-deformation response under quasi-static sinusoidal loading with large deformation.
32	75	0.03	Sinusoidal	15	Assess repeatability of force-deformation response under quasi-static sinusoidal loading with large deformation.
33	75	0.53	Sinusoidal	46	Assess force-deformation response under dynamic sinusoidal loading with large deformation after quasi-static sinusoidal loading history.
34	75	0.53	Sinusoidal	5	Assess repeatability of force-deformation response under dynamic sinusoidal loading with large deformation.
35	75	0.03	Sinusoidal	14	Assess force-deformation response under quasi-static sinusoidal loading with large deformation after dynamic sinusoidal loading history.
36	50	0.04	Sinusoidal	12	Assess repeatability of force-deformation response under quasi-static sinusoidal loading with moderate deformation.
37	50	1.26	Sinusoidal	7	Assess force-deformation response under dynamic sinusoidal loading with moderate deformation after quasi-static sinusoidal loading.
38	50	0.04	Sinusoidal	124	Assess force-deformation response under quasi-static sinusoidal loading with moderate deformation after dynamic sinusoidal loading and large t_{dwell}.
39	50	1.26	Sinusoidal	8	Assess repeatability of force-deformation response observed in test 37.
40	70	–	Earthquake	13	Assess repeatability of force-deformation response observed in test 30.
41	20	0.08	Sinusoidal	25	Assess force-deformation response under quasi-static sinusoidal loading with small deformation.
42	20	1.59	Sinusoidal	57	Assess force-deformation response under dynamic sinusoidal loading with small deformation.
43	10	3.18	Sinusoidal	8	Assess force-deformation response under dynamic sinusoidal loading with small deformation.
44	20	0.08	Sinusoidal	6	Assess repeatability of force-deformation response observed in test 41.
45	70	–	Earthquake	482,000	Assess repeatability of force-deformation response observed in tests 30 and 40 for $t_{\mathrm{dwell}} = 11$ months.

Figure 13A to D compares the FD force-deformation response from tests 30 and 40, tests 31 and 32, tests 33 and 34, and tests 40, 45, and 51, respectively. The dashed lines represent $\pm F_s$. The break-in effect is assessed by comparing the results from tests 30 and 40. Tests 30 and 40 use the same u_{FD}, which is the top floor connection deformation response of the 12-story example building model presented in Tsampras et al,[1] subjected to the 1992 Landers earthquake Coolwater station ground motion, scaled to the DBE level. Figure 13A shows that the FD force-deformation response is similar in tests 30 and 40. Figure 13B shows the repeatability of the FD force-deformation response in quasi-static tests 31 and 32. F_{FDs} in tests 31 and 32 is approximately equal to $1.10F_s$. Figure 13C shows the repeatability of the FD force-deformation response in dynamic tests 33 and 34. F_{FDs} in the last cycles of tests 33 and 34 is approximately $0.85F_s$. The repeatability of the FD force-deformation response after 11 months without sliding (ie, $t_{\mathrm{dwell}} = 11$ months) and without retightening the friction bolts is assessed by comparing the results from tests 40 and 45. Figure 13D shows that the F_{FDs} in test 45 is approximately 15% less than F_{FDs} in test 40. In test 51, the friction bolts were retightened to the same force level as at

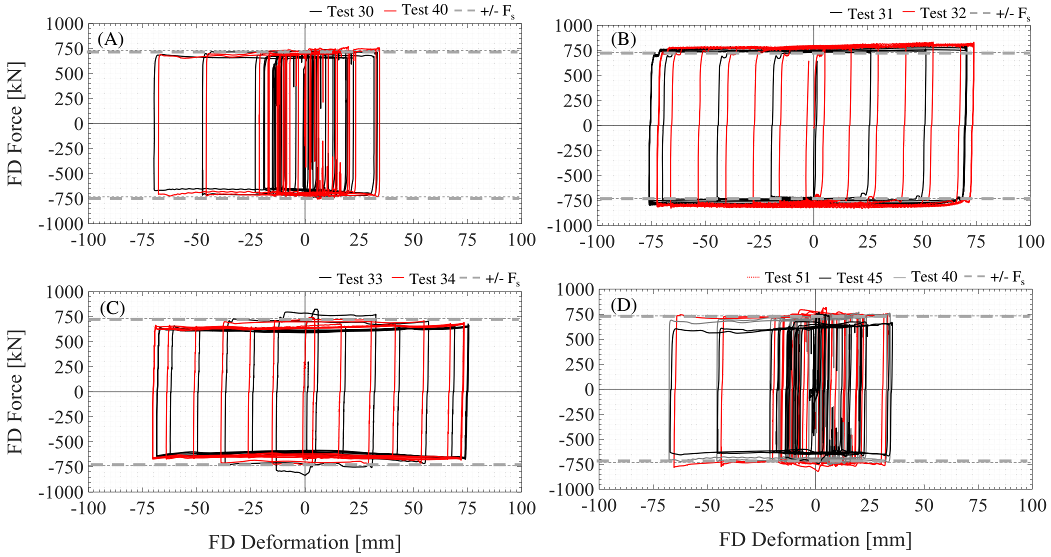

FIGURE 13 Friction device (FD) force-deformation responses [Colour figure can be viewed at wileyonlinelibrary.com]

the beginning of test 30. The FD force-deformation response in test 51 is similar to the FD force-deformation response in test 40. Thus, the F_{FDs} reduction in test 45 is attributed to the loss of friction bolt force during the 11-month dwell time.

Figure 14A shows the $|F_{\mathrm{FD}}|$ time history plotted versus the normalized time, which is defined as the current time during the test divided by the total test time for tests 30 through 44. The test number is shown on the *x*-axis instead of the normalized time. The dashed red lines correspond to F_s, $1.10F_s$, and $0.85F_s$. Figure 14B to D shows the absolute FD deformation $|u_{\mathrm{FD}}|$, absolute FD velocity $|v_{\mathrm{FD}}|$, and the cumulative $|u_{\mathrm{FD}}|$, respectively.

Figure 14 shows the effect of the FD sliding history on $|F_{\mathrm{FDs}}|$ and can be summarized as follows (specific examples are given later): (1) $|F_{\mathrm{FDs}}|$ increases from approximately $0.92F_s$ to approximately $1.00F_s$ due to the "break-in" effect; (2) $|F_{\mathrm{FDs}}|$ in quasi-static tests that follow dynamic tests or earthquake tests increases to approximately $1.10F_s$; (3) $|F_{\mathrm{FDs}}|$ in quasi-static tests that follow quasi-static tests remains approximately equal to $1.10F_s$ (4) $|F_{\mathrm{FDs}}|$ in dynamic tests that follow quasi-static tests decreases from approximately $1.10F_s$ to approximately $0.85F_s$; (5) $|F_{\mathrm{FDs}}|$ in dynamic tests that follow dynamic tests reduces from approximately $1.00F_s$ to approximately $0.85F_s$; (6) $|F_{\mathrm{FDs}}|$ increases to approximately $1.00F_s$ after dynamic tests during t_{dwell}; and (7) t_{dwell} after quasi-static tests does not affect $|F_{\mathrm{FDs}}|$. For example, the "break-in" effect is shown in test 30. $|F_{\mathrm{FDs}}|$ increases from approximately $1.00F_s$ to approximately $1.10F_s$ during quasi-static tests 31, 35, 38, 41, and 44. $|F_{\mathrm{FDs}}|$ remains approximately $1.10F_s$ in quasi-static tests 32 and 36 that followed quasi-static tests 31 and 35. t_{dwell} between quasi-static tests 31 and 32 and t_{dwell} between quasi-static tests 35 and 36 did

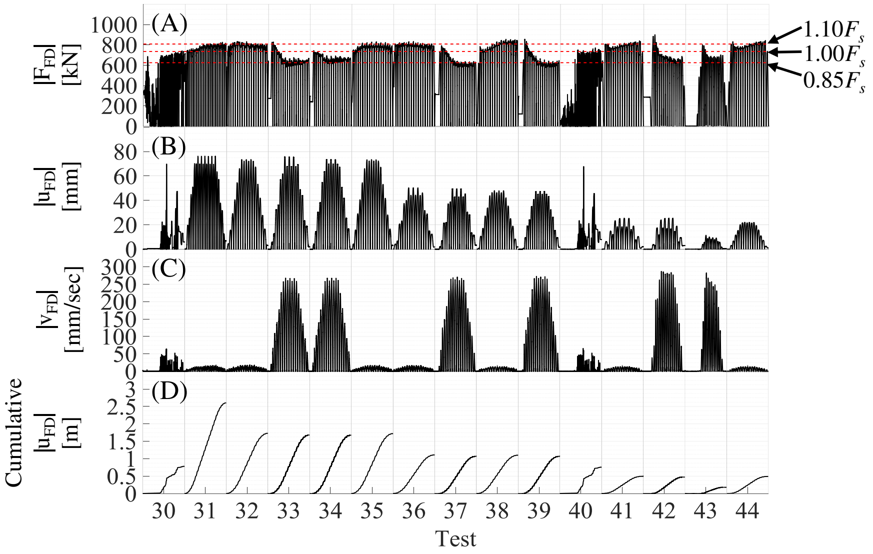

FIGURE 14 A, $|F_{\mathrm{FD}}|$; B, $|u_{\mathrm{FD}}|$; C, $|v_{\mathrm{FD}}|$; D, cumulative $|u_{\mathrm{FD}}|$ histories in tests 30 to 44 [Colour figure can be viewed at wileyonlinelibrary.com]

not affect $|F_{\mathrm{FDs}}|$. $|F_{\mathrm{FDs}}|$ in the first cycles of dynamic tests 33, 37, and 39 is approximately $1.10F_s$, which is approximately equal to $|F_{\mathrm{FDs}}|$ observed in the last cycles of quasi-static tests 32, 36, and 38. Within the duration of dynamic tests 33, 34, 37, and 39 $|F_{\mathrm{FDs}}|$ decreases to approximately $0.85F_s$. $|F_{\mathrm{FDs}}|$ increases from approximately $0.85F_s$ to approximately $1.00F_s$ during t_{dwell} between dynamic tests 33 and 34. The increased $|F_{\mathrm{FDs}}|$ due to t_{dwell} can be observed at the beginning of every test (ie, 34, 35, 38, 40, and 43) that follows a dynamic test.

Test 43 with 3.18-Hz loading frequency has slightly higher $|F_{\mathrm{FDs}}|$ than tests 37 and 39 with 1.26-Hz loading frequency. The temperature of the steel plates was measured at the beginning and at the end of each test by using infrared thermometer. There was no correlation between the temperature variation and the FD force variation.

Figure 15A and B presents more information about the FD force variation observed in dynamic tests. Figure 15A shows with solid line the $|v_{\mathrm{FD}}|$ time history normalized by a reference velocity $v_{\mathrm{ref}} = 250$ mm/s. The blue diamonds show the peak v_{FD}, denoted as $v_{\mathrm{FD,peak}}$, in each half-cycle of the sinusoidal loading normalized by v_{ref}. The red circles show the progression of the maximum normalized $v_{\mathrm{FD,peak}}$. Between 7 seconds and 8 seconds, the overall (for the test) maximum $v_{\mathrm{FD,peak}}$ is reached. Figure 15B shows with a dashed line the $|F_{\mathrm{FD}}|$ time history normalized by F_s. The solid black line shows $\mu_{\mathrm{exp}} = |F_{\mathrm{FDs}}|/2\,N$ normalized by $\mu_s = 0.45$. The mean value of $\mu_{\mathrm{exp}}/\mu_{\mathrm{s}}$ (for each half cycle of response) is shown with an open square. The mean value of $\mu_{\mathrm{exp}}/\mu_{\mathrm{s}}$ at the beginning of the test is approximately 1.00. The mean value of $\mu_{\mathrm{exp}}/\mu_{\mathrm{s}}$ between 7 and 8 seconds is approximately 0.85. The mean value of $\mu_{\mathrm{exp}}/\mu_{\mathrm{s}}$ near the end of the test is approximately 0.89. The results in Figure 15 are summarized as follows: (1) μ_{exp} does not depend on the instantaneous v_{FD}; (2) μ_{exp} decreases as the maximum $v_{\mathrm{FD,peak}}$ increases; (3) a small recovery of μ_{exp} is observed in the last few cycles, when $v_{\mathrm{FD,peak}}$ is less than the maximum $v_{\mathrm{FD,peak}}$; and (4) μ_{exp} is restored back to approximately $1.0\mu_s$ during t_{dwell} between tests 34 and 35. Figure 15C shows all the mean values of μ_{exp} versus the maximum $v_{\mathrm{FD,peak}}$ in tests 30 through 44. The variation of mean μ_{exp} with respect to the maximum $v_{\mathrm{FD,peak}}$ approximately between $0.85\mu_s$ and $1.10\mu_s$ is due to the variation of $|F_{\mathrm{FDs}}|$ discussed above.

Researchers have shown that contacting asperities of the friction interface form the true contact area, which is smaller than the total interface area, and that the adhesion of the junctions is the main source of friction force.[53-56] Changes to the condition of the true contact area, based on the sliding history, are responsible for friction force variation.[57,58] The increase of friction force during t_{dwell} under normal force has been discussed in Bowden and Tabor, Rabinowicz, Dieterich and Kilgore, Courtney-Pratt and Eisner, Rubinstein et al, and Ben-David et al.[54,56,58-61] The progressive increase of friction force under low sliding velocity has been discussed in Rabinowicz, Bar-Sinai et al, and Burwell and Rabinowicz.[56,57,62,63] The reduction of the friction force due to increasing sliding velocity has been discussed in Rabinowicz, Ben-David et al, Burwell and Rabinowicz, and Sampson et al.[56,57,61,63,64]

This paper does not address friction phenomena at the microscale level. However, considering the experimental observations made above, and observations in the literature, the authors suggest the following physical explanation for the $|F_{\mathrm{FDs}}|$ variation. Under large constant N, the asperities at the friction interface deform plastically, and the true contact area increases to A_{jo} until equilibrium is achieved (see Bowden and Tabor, and Tabor[54,55]) at a normal pressure p_{jo}, as schematically shown for a single junction in Figure 16A. Neglecting the break-in effects and considering an interface shear strength s_{jo}, the $|F_{\mathrm{FDs}}|$ associated with this state is assumed to be $1.00F_s$. Under large constant N and small $v_{\mathrm{FD,peak}}$, the junctions at the friction interface grow, the true contact area grows from A_{jo} to A_j, the normal pressure decreases from p_{jo} to p_j, and $|F_{\mathrm{FDs}}|$ increases from $1.00F_s$ to $1.10F_s$, as shown in Figure 16B. This is a new interfacial equilibrium condition with true contact area A_j larger than A_{jo} and normal pressure p_j smaller than p_{jo}. Under large

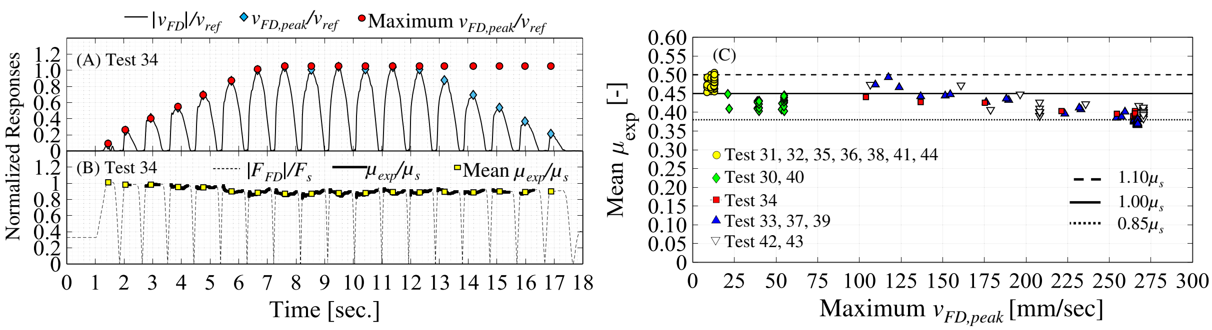

FIGURE 15 A, Time histories of normalized $|v_{\mathrm{FD}}|$, normalized $v_{\mathrm{FD,peak}}$, and normalized maximum $v_{\mathrm{FD,peak}}$; B, time histories of normalized $|F_{\mathrm{FD}}|$, normalized μ_{exp}, and mean normalized μ_{exp}; C, mean μ_{exp} versus maximum $v_{\mathrm{FD,peak}}$ in tests 30 through 44 [Colour figure can be viewed at wileyonlinelibrary.com]

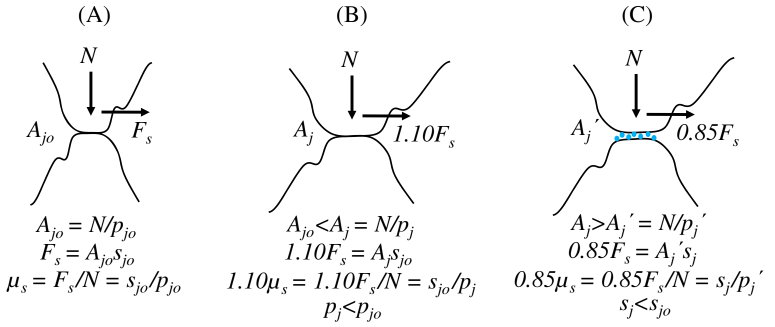

FIGURE 16 Schematic description of a physical explanation for the $|F_{\mathrm{FDs}}|$ variation [Colour figure can be viewed at wileyonlinelibrary.com]

constant N and large $v_{\mathrm{FD,peak}}$, the wear volume[65] and the average wear particle diameter[56] are thought to be larger than the wear volume and the average wear particle diameter under small $v_{\mathrm{FD,peak}}$. The wear particle debris forms a thin film,[66] shown as blue dots in Figure 16C, which is responsible for reducing the interface shear strength from s_{jo} to s_j[54] and possibly reducing the true contact area from A_j to A_j'. As a result, $|F_{\mathrm{FDs}}|$ reduces from $1.10F_s$ to $0.85F_s$. t_{dwell} permits rejuvenation of the friction interface.[61]

Table 4 shows the approximate $|F_{\mathrm{FDs}}|$, N, and μ_{exp} from tests 50 through 55 (ie, sinusoidal tests with applied amplitude 75 mm and frequency 0.03 Hz), which were used to evaluate the FD force-deformation response under different N. The pretension load of the friction bolts was estimated by using an ultrasonic deformation measurement. As N increases, μ_{exp} decreases from 0.47 to 0.40. Figure 17A shows the FD force-deformation response for dynamic test 58 (ie, sinusoidal test with applied amplitude 75 mm and frequency 0.32 Hz) and quasi-static test 60 (ie, sinusoidal test with applied amplitude 75 mm and frequency 0.03 Hz), conducted with $N = 1375$ kN. With $\mu s = 0.40$ (based on μ_{exp} in test 53), $F_s = 1100$ kN. The FD force-deformation responses in tests 58 and 60 are similar to the FD force-deformation response

TABLE 4 Approximate $|F_{\mathrm{FDs}}|$, N, and μ_{exp} in tests 50 through 55

Test	$\lvert F_{\mathrm{FDs}}\rvert$	^1N	$\mu_{\mathrm{exp}} = \lvert F_{\mathrm{FDs}}\rvert/2\,N$
[−]	[kN]	[kN]	[−]
50	620	654	0.47
51	730	812	0.45
52	930	1087	0.43
53	1100	1375	0.40
54	1310	1640	0.40
55	1310	1640	0.40

^1N was estimated by using an ultrasonic deformation measurement method.

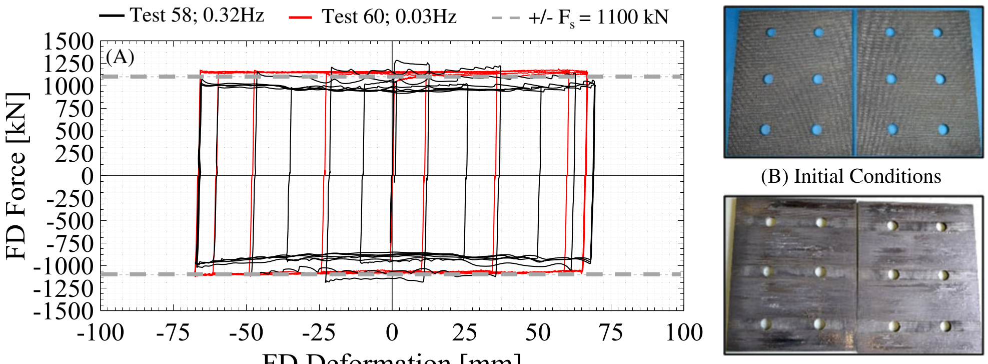

(B) Initial Conditions

(C) End Conditions

FIGURE 17 A, Friction device (FD) force-deformation response with $N = 1375$ kN under quasi-static and dynamic sinusoidal loading histories; condition of friction shims B, at the beginning of test program and C, at the end of test program [Colour figure can be viewed at wileyonlinelibrary.com] observed in previous tests. Figure 17B and C shows the conditions of the friction shims before test 30 (at the beginning) and after test 63 (at the end) of the test program, respectively. No damage to the friction shim holes was observed.

5 | FRICTION DEVICE + RUBBER BEARINGS EXPERIMENTAL RESPONSE

This section summarizes the FD + RB connection force-deformation response, including (1) the overall experimental FD + RB connection force-deformation response; (2) the post-elastic stiffness contribution of RB to the FD + RB connection force-deformation response; (3) the agreement of the FD + RB connection post-elastic force-deformation response with $K_{\text{eff}}D_c + F_s$ and $K_{\text{eff}}D_c - F_s$, where D_c is the FD + RB connection deformation; and (4) the hysteretic energy dissipation contribution of the FD and RB to the FD + RB connection response.

Figure 18A to C shows with solid lines the FD + RB, FD, and RB force-deformation responses in PS3, test 34, and test 60, respectively. The dashed lines show $\pm F_s$, $K_{\text{eff}}D_c$, and $K_{\text{eff}}D_c \pm F_s$, respectively. The elastic stiffness of the FD + RB connection is approximately 1730 kN/mm, which is controlled by the elastic stiffness of the FD. The post-elastic stiffness of the FD + RB connection is controlled by K_{eff}. The force when the FD + RB force-deformation response transitions from elastic to post-elastic is determined by F_s. Figure 18A shows stable FD + RB force-deformation response under quasi-static loading with significant post-elastic stiffness. The friction shims in PS3 were damaged, as shown in Figure 10C, but the damage did not affect significantly the overall FD + RB force-deformation response, as shown in Figure 18A. Figure 18B shows stable FD + RB force-deformation response under dynamic loading. Figure 18C shows

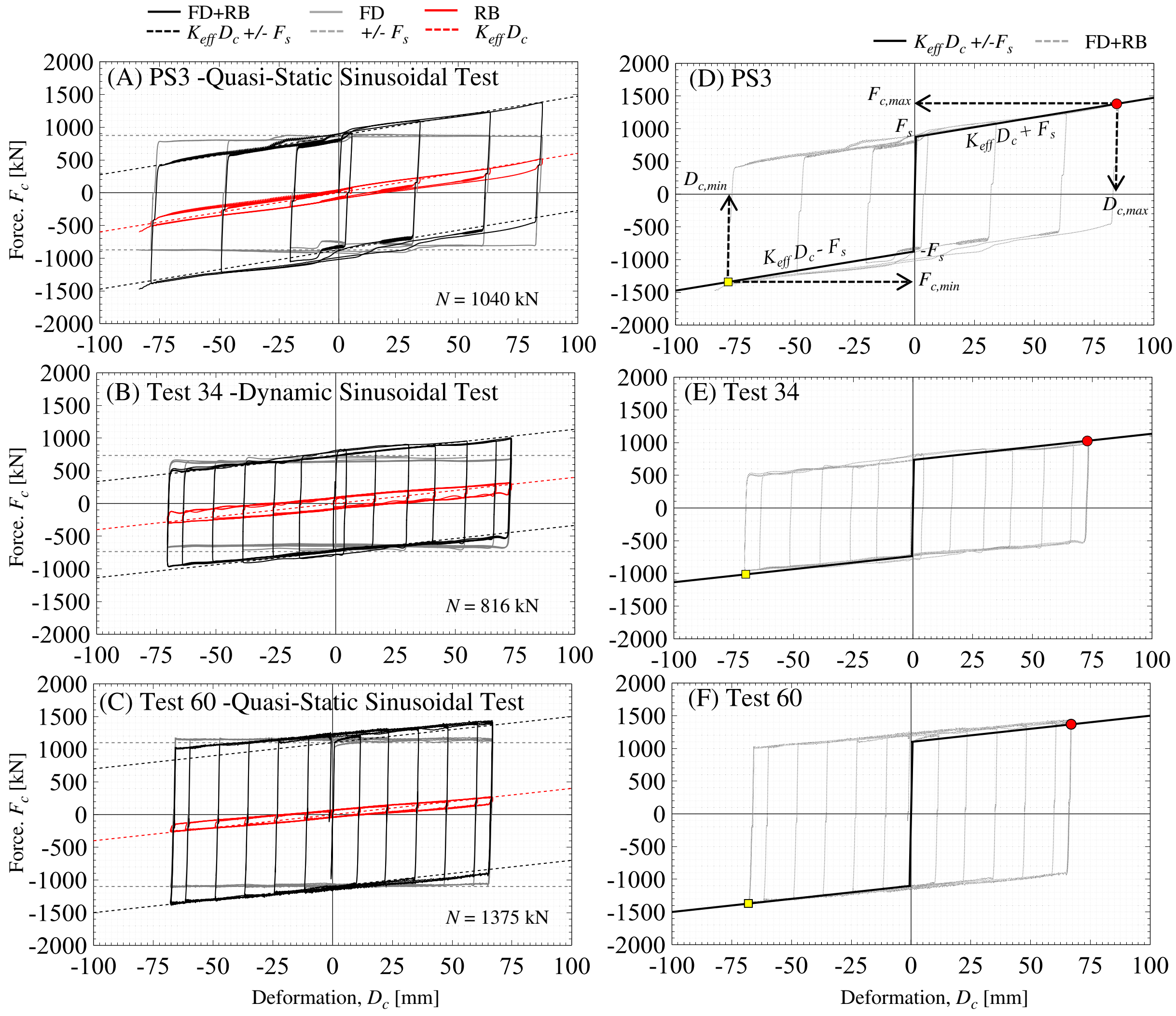

FIGURE 18 Friction device (FD) + rubber bearings (RB), FD, and RB force-deformation responses and $\pm F_s$, K_{eff} D_c, and K_{eff} $D_c \pm F_s$ [Colour figure can be viewed at wileyonlinelibrary.com]

stable FD + RB force-deformation response for a greater value of N, resulting in a greater FD + RB connection force compared with the previous tests. Figure 18D to F shows with dashed lines the FD + RB connection force-deformation response and with solid lines the value of $K_{\mathrm{eff}}D_c \pm F_s$ for PS3, test 34, and test 60, respectively. $K_{\mathrm{eff}}D_c \pm F_s$ is a good approximation to the FD + RB connection post-elastic force-deformation responses from the tests. Table 5 lists the minimum FD + RB force, $F_{c,\mathrm{min}}$; the maximum FD + RB force, $F_{c,\mathrm{max}}$; the minimum FD + RB deformations, $D_{c,\mathrm{min}}$; the maximum FD + RB deformation, $D_{c,\mathrm{max}}$; K_{eff} (see Figure 4); F_s; $K_{\mathrm{eff}}D_{c,\mathrm{max}} + F_s$; and $K_{\mathrm{eff}}D_{c,\mathrm{min}} - F_s$, for PS3, test 34, and test 60. The results in Figure 18 and Table 5 show that a bilinear elastic-plastic model with kinematic hardening will accurately simulate the FD + RB connection force-deformation response.

Figure 19A and B shows the FD + RB connection and FD hysteretic energy time histories from tests 34 and 60, respectively. The total FD + RB connection hysteretic energy dissipation is similar to the FD hysteretic energy dissipation in both tests. The difference, which equals the RB hysteretic energy dissipation, is insignificant compared with the FD hysteretic energy dissipation.

6 | NUMERICAL EARTHQUAKE SIMULATIONS AT SYSTEM LEVEL

In this section, a limited numerical study is presented to assess the effect of potential variations in the FD + RB connection force response on the seismic response of a 12-story reinforced concrete shear-wall building with identical FD + RB connections between at each floor and the shear wall. The site is a generic seismic design classification D with soil class D.[67] The portion of the effective seismic weight of the building assigned to each level x is equal to 10,809 kN. The ASCE 7 design base shear is equal to 20,030 kN. The models for the shear wall and GLRS in the model for the building are described in Tsampras et al.[1] The first 3 periods of vibration of the building are $T_1 = 1.49$ second, $T_2 = 0.24$ second, and $T_3 = 0.09$ second. As noted in Tsampras et al,[1] a damping coefficient was not assigned to the wall base nonlinear spring or to the elements that represent the deformable connections. Three variations on the building models are studied in this section with 3 different FD + RB connection force-deformation models. The 3 FD + RB connection models have bilinear elastic-plastic force deformation response with kinematic hardening. For the 3 models, the force at the transition from elastic to post-elastic response is $1.10F_s$, $1.00F_s$, and $0.85F_s$, respectively, where $F_s = 1270$ kN, assuming $n_s = 2$, $\mu_s = 0.4$, and $N = 1588$ kN. $|F_{\mathrm{FDs}}|$ values in tests 53, 54, and 55 listed in Table 4 are similar to F_s considered in this numerical study. For each model, the elastic stiffness is 1730 kN/mm and the post-elastic stiffness is 6.8 kN/mm. The building models with FD + RB connection models with $1.10F_s$, $1.00F_s$, and $0.85F_s$ are denoted as the 1.10FD + RB building model, the 1.00FD + RB building model, and the 0.85FD + RB building model, respectively.

TABLE 5 Friction device (FD) + rubber bearings (RB) experimental response quantities and post-elastic force predictions

	$F_{c,\mathrm{min}}$	$F_{c,\mathrm{max}}$	$D_{c,\mathrm{min}}$	$D_{c,\mathrm{max}}$	K_{eff}	F_s	$K_{\mathrm{eff}}\ D_{c,\mathrm{min}}$-$F_s$	$K_{\mathrm{eff}}\ D_{c,\mathrm{max}} + F_s$
	[kN]	[kN]	[mm]	[mm]	[kN/mm]	[kN]	[kN]	[kN]
PS3	−1388	1374	−78	85	6	874	−1342	1384
Test 34	−969	1005	−70	73	4	735	−1015	1027
Test 60	−1363	1415	−68	67	4	1100	−1372	1368

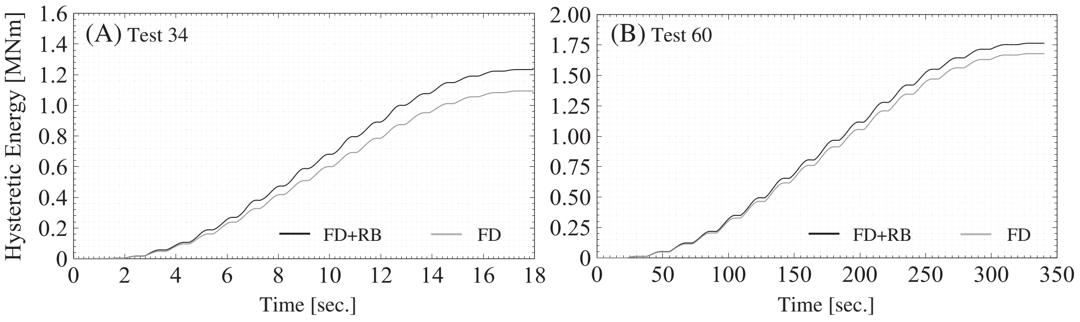

FIGURE 19 Friction device (FD) + rubber bearings (RB) and FD hysteretic energy time histories in A, test 34 and B, test 60

Eighteen ground motions were selected from the FEMA P-695[67] far field set and used as input in the numerical earthquake simulations, as discussed in Tsampras et al.[1] The average method[68] was used to scale these recorded ground motions so the spectral accelerations match the ASCE7-10[69] DBE spectrum over a range of periods $T \in [0.6, 2.0]$ seconds.

Figure 20A through F shows the peak and the mean peak values for the LFRS (ie, shear wall) story shear, floor total acceleration, LFRS story drift, GLRS story drift, FD + RB connection force, and FD + RB connection deformation from the numerical simulations for the set of 18 ground motions, where "peak" refers to the maximum absolute value from the time history response at each floor (or story) and "mean" refers to the mean value for the set of ground motions. Table 6 lists the maximum mean peak values of the responses and their standard deviations, where "maximum" refers to the maximum mean peak over all floors (or stories). The maximum mean peak responses are similar for the 3 building models. However, the FD + RB connection deformation demand is larger for the 0.85FD + RB building model compared with the 1.00FD + RB and 1.10FD + RB building models. Although peak LFRS story drifts and FD + RB connection

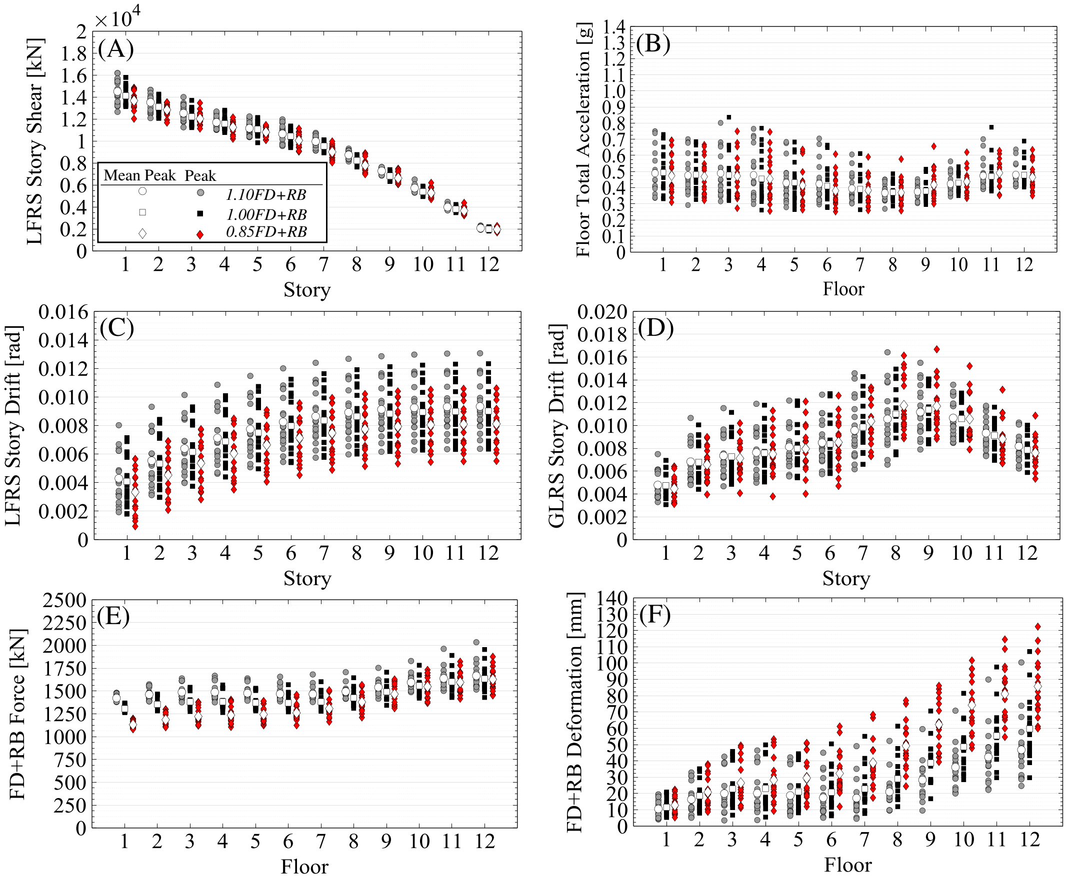

FIGURE 20 Sensitivity numerical study results [Colour figure can be viewed at wileyonlinelibrary.com]

TABLE 6 Maximum mean peak responses and their standard deviations (σ) for each building model

	LFRS Story Shear		Total Floor Acceleration		LFRS Story Drift		GLRS Story Drift		FD + RB Force		FD + RB Deformation	
	Mean [kN]	σ [kN]	Mean [g]	σ [g]	Mean [rad]	σ [rad]	Mean [rad]	σ [rad]	Mean [kN]	σ [kN]	Mean [mm]	σ [mm]
1.10FD + RB	14,678	1,170	0.48	0.06	0.0094	0.0019	0.011	0.0026	1,690	120	43	18
1.00FD + RB	14,296	885	0.48	0.08	0.0092	0.0018	0.011	0.0025	1,646	133	56	20
0.85FD + RB	13,807	770	0.46	0.08	0.0084	0.0016	0.012	0.0024	1,628	125	81	18
Rigid elastic	28,156	10,385	1.33	0.58	0.0110	0.0021	0.0110	0.0021	7,113	3485	0	0

FD indicates friction device; GLRS, flexible gravity load resisting system; LFRS, lateral force resisting system; RB, rubber bearings.

force demands are slightly lower for the 0.85FD + RB building model compared with the 1.00FD + RB and 1.10FD + RB building models, larger FD + RB connection deformation demands are expected for the former case.

Table 6 also lists the maximum mean peak responses and their standard deviations for the case that rigid elastic connections are used instead of deformable connections, as reported in Tsampras et al.[1] The force and acceleration responses are significantly reduced when deformable connections are used instead of rigid elastic connections. A detailed comparison is presented in Tsampras et al.[1]

7 | CONCLUSIONS

This paper has presented experimental and numerical studies of a full-scale deformable connection used to connect the floor system of the flexible GLRS to the stiff LFRS of an earthquake-resistant building. The purpose of the deformable connection is to limit the earthquake-induced horizontal inertia force transferred from the floor system to the LFRS and thereby to reduce the horizontal floor accelerations and the forces in the LFRS. The deformable connection that was studied consists of an FD and carbon fiber-reinforced laminated low-damping RB, denoted as the FD + RB connection. The paper presented details of an FD + RB connection test specimen. The experimental response of the FD, which dominated the FD + RB connection force-deformation response, was discussed extensively. The paper presented results from preliminary experimental studies of FD force variation, which compare low levels of normal force versus high levels of normal force, and machined steel components with tight tolerances versus steel components with mill-quality surfaces and looser tolerances. The paper also presented more detailed information about FD force variation observed in quasi-static and dynamic tests and the relationship of the FD force variation to the FD interface sliding history. Finally, a validated, reasonably accurate model for the FD + RB connection force-deformation response was presented. Results from limited numerical simulations using this model were presented to assess the effects of potential FD force variations on the seismic response of a 12-story reinforced concrete shear-wall building model.

Conclusions from the experimental studies and limited numerical simulations are as follows:

1. The experimental results show that the FD + RB connection has stable force-deformation response under quasi-static sinusoidal and earthquake loading histories and dynamic sinusoidal loading histories.
2. The FD + RB force-deformation response can be modeled with reasonable accuracy by using a bilinear elastic-plastic model with kinematic hardening.
3. The RB provide predictable and reliable post-elastic stiffness to the FD + RB connection force-deformation response. The RB force-deformation response is not sensitive to the frequency of loading history.
4. The FD developed for the FD + RB connection is axially stiff, compact, easy-to-assemble, and accommodates the FD + RB connection kinematic requirements.
5. The FD elastic stiffness controls the FD + RB elastic stiffness. The FD friction force controls the force when the FD + RB force-deformation response transitions from elastic to post elastic.
6. The “break-in” effect, the sliding history, and the dwell time affect the FD friction force. The approximate variation of the FD friction force is ±15%.
7. The machining tolerances for the FD steel components can affect the FD friction force, but the FD developed in this research for full-scale FD force levels had acceptable FD friction force variations (ie, less than 15%) even though its steel components were fabricated with relatively loose tolerances.
8. The main effect of potential FD friction force variations on the seismic response of a 12-story reinforced concrete shear-wall building model with FD + RB connections is on the FD + RB connection deformation demands, which increase as the FD friction force decreases.

ACKNOWLEDGEMENTS

This paper is based upon work supported by grants from the National Science Foundation, award no. CMMI-1135033 in the George E. Brown, Jr. Network for Earthquake Engineering Simulation Research (NEESR) program and award no. CMMI-0402490 for the George E. Brown, Jr. Network for Earthquake Engineering Simulation (NEES) consortium operations. The authors are grateful for additional financial support provided by the Gerondelis Foundation, Yen Fellowship, and Lehigh University. The contributions of Dr Joe Maffei, Mr David Mar, Dr Shivaglal Cheruvalath, and the NEES@Lehigh and ATLSS Center staff are acknowledged. The authors appreciate the contribution of the companies DYMAT™, Star Seismic®, and Scan-Pac Mfg, Inc. Any opinions, findings, and conclusions expressed in this report are those of the authors and do not necessarily reflect the views of the National Science Foundation or others acknowledged here.

ORCID

Georgios Tsampras http://orcid.org/0000-0001-8255-3415

REFERENCES

1. Tsampras G, Sause R, Zhang D, et al. Development of deformable connection for earthquake-resistant buildings to reduce floor accelerations and force responses. *Earthquake Engineering and Structural Dynamics*. 2016;45(9):1473-1494. https://doi.org/10.1002/eqe.2718
2. Tsampras G, Sause R. "Development and experimental validation of deformable connection for earthquake-resistant building systems with reduced floor accelerations," Network of Earthquake Engineering Simulation (NEES) Technical Report, https://nees.org/resources/13612, 2015.
3. Zhang D, Fleischman R, Restrepo J, et al. "Development of a floor inertia force limiting anchorage system under earthquake loading," in 10th U.S. National Conference on Earthquake Engineering (10NCEE)/NEES Quake Summit, Anchorage, AK, 2014.
4. Fleischman R, Restrepo J, Nema A, et al. Inertial force-limiting anchorage system for seismic resistant building structures. In: *2015 Structures Congress*. OR: Portland; 2015.
5. Constantinou M, Whittaker A, Kalpakidis Y, Fenz D, Warn G. "Performance of seismic isolation hardware under service and limit loading," State of California Department of Transportation Project, 2007.
6. Naeim F, Kelly JM. Design of seismic isolated structures: from theory to practice, John Wiley & Sons, Inc., 1999.
7. Kelly JM, Takhirov SM. "Analytical and experimental study of fiber-reinforced elastomeric isolators," PEER 2001/11, Berkeley, CA, 2001.
8. Huang Y-N, Whittaker AS, Luco N. Seismic performance assessment of base-isolated safety-related nuclear structures. *Earthquake Engineering and Structural Dynamics*. 2010;39(13):1421-1442. https://doi.org/10.1002/eqe.1038
9. AASHTO. LRFD bridge design specification, Washington, DC, 2010.
10. AASHTO. "Guide specifications for seismic isolation design," 2010.
11. Kelly J, Konstantinidis D. Mechanics of rubber bearings for seismic and vibration isolation, John Wiley and Sons Ltd, 2011.
12. Lindley P. "Engineering design with natural rubber, NR technical bulletins," The Malaysian Rubber Producers' Research Association, 1978.
13. Clark P, Bassett R, Bradshaw J. Plate friction load control devices—their application and potential. *ICE Proceedings*. 1973;55(2):335-352.
14. Loo Y, Upfold RBD. The behavior of an earthquake energy absorber for bridge decks. In: *Sixth Australian Conference on the Mechanics of Structures and Materials*. Christchurch, New Zealand, August 22-24: University of Canterbury; 1977.
15. Pall AS. "Limited slip bolted joints—a device to control seismic response of large panel structures," PhD Dissertation, Concordia University, 1979.
16. Bora C, Oliva MG, Nakaki SD, Becker R. Development of a precast concrete shear-wall system requiring special code acceptance. *PCI Journal*. 2007;52(1):122-135. https://doi.org/10.15554/pcij.01012007.122.135
17. Morgen BG. "Friction-damped unbonded port-tensioned precast concrete moment frame structures for seismic regions," PhD Dissertation, University of Notre Dame, 2007.
18. Morgen BG, Kurama YC. Seismic response evaluation of posttensioned precast concrete frames with friction dampers. *Journal of Structural Engineering*. 2008;134(1):132-145. https://doi.org/10.1061/(ASCE)0733-9445(2008)134:1(132)
19. Song L-l, Guo T, Chen C. Experimental and numerical study of a self-centering prestressed concrete moment resisting frame connection with bolted web friction devices. *Earthquake Engineering and Structural Dynamics*. 2014;43(4):529-545. https://doi.org/10.1002/eqe.2358
20. Pall AS, Marsh C. Response of friction damped braced frames. *Journal of the Structural Division*. 1982;108(6):1313-1323.
21. Baktash P, Marsh C. "Seismic behavior of friction damped braced frames," in Proceedings of the third U.S. National Conference on Earthquake Engineering, Charleston, SC, August 24-28, 1986.
22. Filiatrault A, Cherry M. Performance evaluation of friction damped braced steel frames under simulated earthquake loads. *Earthq Spectra*. 1987;3(1):57-78. https://doi.org/10.1193/1.1585419
23. Aiken I, Kelly J, Pall A. "Seismic response of a nine-story steel frame with friction-damped cross-bracing," Report No. UCB / EERC-88/17, Earthquake Engineering Research Center, the University of California at Berkeley, 1988.
24. Anagnostides G. "Design of economical means of enhancing the energy-absorption capability of braced frame structures," PhD Dissertation, University of London, Imperial College of Science and Technology, 1988.

25. Anagnostides G, Hargreaves A. Shake table testing on an energy absorption device for steel braced frames. *Soil Dynamics and Earthquake Engineering*. 1990;9(3):120-140. https://doi.org/10.1016/S0267-7261(09)90012-4
26. FitzGerald TF, Anagnos T, Goodson M, Zsutty T. Slotted bolted connections in aseismic design for concentrically braced connections. *Earthq Spectra*. 1989;5(2):383-391. https://doi.org/10.1193/1.1585528
27. Giacchetti R, Whittaker AS, Bertero VV, Aktan HM. Seismic response of a DMRSF retrofitted with friction-slip devices. *International meeting on base isolation and passice energy dissipation*. 1989;12.01-12.12, June 8-9.
28. Tremblay R. "Seismic behavior and design of friction concentrically braced frames for steel buildings," PhD Dissertation, The Univeristy of British Columbia, 1993.
29. Grigorian CE, Yang TS, Popov EP. Slotted bolted connection energy dissipators. *Earthq Spectra*. 1993;9(3):491-504. https://doi.org/10.1193/1.1585726
30. Grigorian CE, Popov EP. "Energy dissipation with slotted bolted connections," UCB/EERC-94/02, 1994.
31. Khoo H-H, Clifton C, Butterworth J, MacRae G, Ferguson G. Influence of steel shim hardness on the sliding hinge joint performance. *J Constr Steel Res*. 2012;72:119-129. https://doi.org/10.1016/j.jcsr.2011.11.009
32. Petty GD. "Evaluation of a friction component for a post-tensioned steel connection," MSc Thesis, Lehigh University, 1999.
33. Rojas P, Ricles JM, Sause R. Seismic performance of post-tensioned steel moment resisting frames with friction devices. *Journal of Structural Engineering*. 2005;131(4):529-540. https://doi.org/10.1061/(ASCE)0733-9445(2005)131:4(529)
34. Tsai K-C, Chou C-C, Lin C-L. Seismic self-centering steel beam-to-column moment connections using bolted friction devices. *Earthquake Engineering and Structural Dynamics*. 2007;37:627-645.
35. Kim H-J, Christopoulos C. Friction damped posttensioned self-centering steel moment-resisting frames. *Journal of Structural Engineering*. 2008;134(11):1768-1779. https://doi.org/10.1061/(ASCE)0733-9445(2008)134:11(1768)
36. Wolski M, Ricles JM, Sause R. Experimental study of a self-centering beam-column connection with bottom flange friction device. *Journal of Structural Engineering*. 2009;135(5):479-488. https://doi.org/10.1061/(ASCE)ST.1943-541X.0000006
37. Lin Y-C, Sause R, Ricles J. Seismic performance of a large-scale steel self-centering moment-resisting frame: MCE hybrid simulations and quasi-static pushover tests. *Journal of Structural Engineering*. 2013;139(7):1227-1236. https://doi.org/10.1061/(ASCE)ST.1943-541X.0000661
38. Loo WY, Kun C, Quenneville P, Chouw N. Experimental testing of a rocking timber shear wall with slip-friction connectors. *Earthquake Engineering and Structural Dynamics*. 2014;43(11):1621-1639. https://doi.org/10.1002/eqe.2413
39. Tyler R. Test on brake lining damper for structures. *Bulletin of New Zealand National Society for Earthquake Engineering*. 1985;18(3):280-284.
40. Aiken ID, Kelly JM. "Earthquake simulator testing and analytical studies of two energy-absorbing systems for multistory structures," Report NO. UCB/EERC-90/03, Earthquake Engineerign Research Center, University of California Berkeley, p. 276, 1990.
41. Aiken DI, Nims DK, Whittaker AS, Kelly JM. Testing of passive energy dissipation systems. *Earthq Spectra*. 1993;9(3):335-368. https://doi.org/10.1193/1.1585720
42. Nims DK, Richter PJ, Bachman RE. The use of the energy dissipating restraint for seismic hazard mitigation. *Earthq Spectra*. 1993;9(3):467-489. https://doi.org/10.1193/1.1585725
43. Filiatrault A, Tremblay R, Kar R. Performance evaluation of friction spring seismic damper. *Journal of Structural Engineering*. 2000;126(4):491-499. https://doi.org/10.1061/(ASCE)0733-9445(2000)126:4(491)
44. Zhu S. "Seismic behavior of framed structural system with self-centering friction damping braces," PhD Dissertation, Lehigh University, 2007.
45. Christopoulos C, Tremblay R, Kim H-J, Lacerte M. Self-centering energy dissipative bracing system for the seismic resistance of structures: development and validation. *Journal of Structural Engineering 134, SPECIAL ISSUE: Design and Analysis of Structures with Seismic Damping Systems*. 2008;134(1):96-107. https://doi.org/10.1061/(ASCE)0733-9445(2008)134:1(96)
46. Erochko J, Christopoulos C, Tremblay R. Design and testing of an enhanced-elongation telescoping self-centering energy-dissipative brace. *Journal of Structural Engineering*. 2015;141(6):
47. Chou C-C, Chen Y-C. Development of steel dual-core self-centering braces: quasi-static cyclic tests and finite element analyses. *Earthq Spectra*. 2015;31(1):247-272. https://doi.org/10.1193/082712EQS272M
48. AISC. Steel construction manual, Americal Institute of Steel Construction, 2010.
49. ASTM B36 / B36M-13. "Standard specification for brass plate, sheet, strip, and rolled bar," ASTM International, 2013.
50. Champion Technologies Inc. "Product description and application: AFT-200," Eugene, Oregon, USA, 2008.
51. Chi B, Uang C-M. "Dynamic testing of full-scale slotted bolted connections, report no. TR-99/05," Department of Structural Engineering, University of California, San Diego, 2000.
52. Scan Pan Inc. "Gatke material selection guide," Menomonee Falls, WI, USA, 2010.

53. McFarlane JS, Tabor D. Relation between friction and adhesion. *Proc R Soc Lond A Math Phys Sci*. 1950;202(1069):244-253. https://doi.org/10.1098/rspa.1950.0097
54. Bowden F, Tabor D. *The Friction and Lubrication of Solids*. London: Oxford University Press; 1954.
55. Tabor D. Friction—the present state of our understanding. *Journal of Lubrication Technology*. 1981;103:169-179.
56. Rabinowicz E. *Friction and Wear of Materials*. 2nd ed. John Wiley & Sons, Inc.; 1995.
57. Rabinowicz E. The intrinsic variables affecting the stick-slip process. *Proceedings of the Physical Society London*. 1958;71(4):668-675. https://doi.org/10.1088/0370-1328/71/4/316
58. Dieterich JH, Kilgore BD. Direct observation of frictional contacts: new insights for state-dependent properties. *Pure Appl Geophys*. 1994;143(1-3):283-302. https://doi.org/10.1007/BF00874332
59. Courtney-Pratt JS, Eisner E. The effect of a tangential force on the contact of metallic bodies. *Proc R Soc Lond A Math Phys Sci*. 1957;238(1215):529-550. https://doi.org/10.1098/rspa.1957.0016
60. Rubinstein MS, Cohen G, Fineberg J. Detachment fronts and the onset dynamic friction. *Nature*. 2004;430(26):1005-1009. https://doi.org/10.1038/nature02830
61. Ben-David O, Rubinstein MS, Fineberg J. Slip-stick and the evolution of frictional strength. *Nature*. 2010;463(7):76-78. https://doi.org/10.1038/nature08676
62. Bar-Sinai Y, Spatschek R, Brener EA, Bouchbinder E. On the velocity-strengthening behavior of dry friction. *J Geophys Res Solid Earth*. 2014;119(3):1738-1748. https://doi.org/10.1002/2013JB010586
63. Burwell JT, Rabinowicz E. The nature of the coefficient of friction. *J Appl Phys*. 1953;24(2):136-139. https://doi.org/10.1063/1.1721227
64. Sampson JB, Morgan F, Reed DW, Muskat M. Studies in lubrication: XII. Friction behavior during the slip portion of the stick-slip process. *J Appl Phys*. 1943;14(12):689-700. https://doi.org/10.1063/1.1714948
65. Rhee S. Wear or metal-reinforced phenolic resins. *Wear*. 1971;18(6):471-477. https://doi.org/10.1016/0043-1648(71)90171-2
66. Liu T, Rhee SK, Lawson KL. A study of wear rates and transfer films of friction materials. *Wear*. 1980;60(1):1-12. https://doi.org/10.1016/0043-1648(80)90246-X
67. FEMA P695. *Quantification of building seismic performance factors*. Washington, DC: Federal Emergency Management; 2009.
68. Baker JW. Conditional mean spectrum: tool for ground—motion selection. *Journal of Structural Engineering*. 2011;137(3):322-331. https://doi.org/10.1061/(ASCE)ST.1943-541X.0000215
69. ASCE. *ASCE Standard ASCE/SEI7-10: Minimum Design Loads for Buildings and Other Structures*. Reston, Virginia: American Society of Civil Engineers; 2010.

How to cite this article: Tsampras G, Sause R, Fleischman RB, Restrepo JI. Experimental study of deformable connection consisting of friction device and rubber bearings to connect floor system to lateral force resisting system. *Earthquake Engng Struct Dyn*. 2017;1–22. https://doi.org/10.1002/eqe.3004